

AFIT/GAE/ENY/91D-3

AD-A243 916



DTIC
ELECTE
JAN 06 1992
S D D

FINITE ELEMENT ANALYSIS OF A RIVETED
REPAIR ON A CURVED COMPOSITE PANEL

THESIS

Scott A. Hamilton
Second Lieutenant, USAF

AFIT/GAE/ENY/91D-3

92-00055
AD-A243 916

Approved for public release, distribution unlimited

92 1 2 064

20000901 046

AFIT/GAE/ENY/91D-3

**FINITE ELEMENT ANALYSIS OF A RIVETED REPAIR ON A CURVED
COMPOSITE PANEL**

THESIS

**Presented to the Faculty of the School of Engineering
of the Air Force Institute of Technology**

Air University

**In Partial Fulfillment of the
Requirements for the Degree of
Master of Science in Aeronautical Engineering**



Scott A. Hamilton, B.S.

Second Lieutenant, USAF

December, 1991

Accession	
DTIC	
DATE	
UNCLASSIFIED	
Justification	
By	
DATE	
For	
DOI	
A-1	

Approved for public release; distribution unlimited

Acknowledgements

I would like to express my thanks and appreciation to Dr. Palazotto, for his helpful advice; to Dr. Mall, for agreeing to be on my committee in spite of his many other obligations; and finally to Captain Gans, for his patience and help while I pestered and flustered.

And, of course, I would like to thank everyone else who put up with me during this (has it already been so long?) last year and a half.

Table of Contents

	Page
Preface	ii
List of Figures	iv
List of Tables	x
Abstract	xi
I. Introduction	1
Background	2
Methodology	4
II. Theory	7
Overview	7
Laminated Plate Theory	7
Finite Element Method	11
Eigenvalue Analysis	20
III. Finite Element Modeling	24
Laminzate Property Modeling	24
Full Panel Model	26
Cutout Section Model	28
Patch Modeling	31
IV. Results	37
Full Panel Model	37
Cutout Section Models	48
Repaired Panel Models	67
V. Conclusions and Recommendations	100
Bibliography	102
Vita	105

List of Figures

Figure Name	Page Number
Figure 1. Z-axis Rotation Incompatibility	14
Figure 2. Coefficient Triangle	17
Figure 3. ELAS2 Element	19
Figure 4. GAP Element	19
Figure 5. Laminate Properties	25
Figure 6. Full Panel Model	26
Figure 7. Refined Panel Model	27
Figure 8. 0° Cutout Section Model	28
Figure 9. 90° Cutout Section Model	28
Figure 10. +45° Cutout Section Model	30
Figure 11. -45° Cutout Section Model	30
Figure 12. Rivet Placement	34
Figure 13. Close View of Patch	35
Figure 14. Full Panel Model Mode 1, $f = 558$ hz	39
Figure 15. Refined Full Panel Model Mode 1, $f = 550$ hz	39
Figure 16. Full Panel Model Mode 2, $f = 591$ hz	40
Figure 17. Refined Full Panel Model Mode 2, $f = 571$ hz	40
Figure 18. Full Panel Model Mode 3, $f = 761$ hz	41
Figure 19. Refined Full Panel Model Mode 3, $f = 755$ hz	41

Figure 20. Full Panel Model Mode 4, $f = 825$ hz	42
Figure 21. Refined Full Panel Model Mode 4, $f = 820$ hz	42
Figure 22. Full Panel Model Mode 5, $f = 916$ hz	43
Figure 23. Refined Full Panel Model Mode 5, $f = 905$ hz	43
Figure 24. 0° Cutout Section Model Mode 1, $f = 491$ hz	45
Figure 25. 0° Cutout Section Model Mode 2, $f = 560$ hz	45
Figure 26. 0° Cutout Section Model Mode 3, $f = 662$ hz	46
Figure 27. 0° Cutout Section Model Mode 4, $f = 758$ hz	46
Figure 28. 0° Cutout Section Model Mode 5, $f = 812$ hz	47
Figure 29. 0° Cutout Effects	47
Figure 30. 90° Cutout Section Model Mode 1, $f = 578$ hz	50
Figure 31. 90° Cutout Section Refined Model Mode 1, $f = 570$ hz . .	50
Figure 32. 90° Cutout Section Model Mode 2, $f = 582$ hz	51
Figure 33. 90° Cutout Section Refined Model Mode 2, $f = 575$ hz . .	51
Figure 34. 90° Cutout Section Model Mode 3, $f = 716$ hz	52
Figure 35. 90° Cutout Section Refined Model Mode 3, $f = 709$ hz . .	52
Figure 36. 90° Cutout Section Model Mode 4, $f = 765$ hz	53
Figure 37. 90° Cutout Section Refined Model Mode 4, $f = 744$ hz . .	53
Figure 38. 90° Cutout Section Model Mode 5, $f = 779$ hz	54
Figure 39. 90° Cutout Section Refined Model Mode 5, $f = 782$ hz . .	54
Figure 40. 90° Cutout Section Model Mode 6, $f = 802$ hz	55
Figure 41. 90° Cutout Section Refined Model Mode 6, $f = 790$ hz . .	55

Figure 42. 90° Cutout Effects	56
Figure 43. +45° Cutout Section Model Mode 1, f = 556 hz	58
Figure 44. +45° Cutout Section Model Mode 2, f = 592 hz	58
Figure 45. +45° Cutout Section Model Mode 3, f = 711 hz	59
Figure 46. +45° Cutout Section Model Mode 4, f = 753 hz	59
Figure 47. +45° Cutout Section Model Mode 5, f = 823 hz	60
Figure 48. +45° Cutout Section Model Mode 6, f = 850 hz	60
Figure 49. +45° Cutout Effects	61
Figure 50. -45° Cutout Section Model Mode 1, f = 550 hz	63
Figure 51. -45° Cutout Section Model Mode 2, f = 584 hz	63
Figure 52. -45° Cutout Section Model Mode 3, f = 698 hz	64
Figure 53. -45° Cutout Section Model Mode 4, f = 749 hz	64
Figure 54. -45° Cutout Section Model Mode 5, f = 818 hz	65
Figure 55. -45° Cutout Section Model Mode 6, f = 819 hz	65
Figure 56. -45° Cutout Effects	66
Figure 57. Refined 0° Patch Model	67
Figure 58. 0° Repair Individual Rivet Model Mode 1, f = 460 hz	69
Figure 59. 0° Repair Perfect Bond Model Mode 1, f = 537 hz	69
Figure 60. 0° Repair Individual Rivet Model Mode 2, f = 531 hz	70
Figure 61. 0° Repair Perfect Bond Model Mode 2, f = 600 hz	70
Figure 62. 0° Repair Individual Rivet Model Mode 3, f = 702 hz	71
Figure 63. 0° Repair Perfect Bond Model Mode 3, f = 779 hz	71

Figure 64.	0° Repair Individual Rivet Model Mode 4, $f = 780$ hz	72
Figure 65.	0° Repair Perfect Bond Model Mode 4, $f = 928$ hz	72
Figure 66.	0° Repair Individual Rivet Model Mode 5, $f = 830$ hz	73
Figure 67.	0° Repair Perfect Bond Model Mode 5, $f = 954$ hz	73
Figure 68.	0° Repair Individual Rivet Model Mode 6, $f = 853$ hz	74
Figure 69.	0° Repair Perfect Bond Model Mode 6, $f = 992$ hz	74
Figure 70.	0° Repair Refined Rivet Model Mode 1, $f = 447$ hz	75
Figure 71.	0° Repair Refined Rivet Model Mode 2, $f = 522$ hz	75
Figure 72.	0° Repair Refined Rivet Model Mode 3, $f = 689$ hz	76
Figure 73.	0° Repair Refined Rivet Model Mode 4, $f = 757$ hz	75
Figure 74.	0° Repair Refined Rivet Model Mode 5, $f = 815$ hz	77
Figure 75.	0° Repair Refined Rivet Model Mode 6, $f = 849$ hz	77
Figure 76.	0° Repair Effects	78
Figure 77.	90° Repair Individual Rivet Model Mode 1, $f = 475$ hz	80
Figure 78.	90° Repair Perfect Bond Model Mode 1, $f = 592$ hz	80
Figure 79.	90° Repair Individual Rivet Model Mode 2, $f = 506$ hz	81
Figure 80.	90° Repair Perfect Bond Model Mode 2, $f = 616$ hz	81
Figure 81.	90° Repair Individual Rivet Model Mode 3, $f = 710$ hz	82
Figure 82.	90° Repair Perfect Bond Model Mode 3, $f = 817$ hz	82
Figure 83.	90° Repair Individual Rivet Model Mode 4, $f = 759$ hz	83
Figure 84.	90° Repair Perfect Bond Model Mode 4, $f = 955$ hz	83
Figure 85.	90° Repair Individual Rivet Model Mode 5, $f = 828$ hz	84

Figure 86.	90° Repair Perfect Bond Model Mode 5, $f = 978$ hz	84
Figure 87.	90° Repair Effects	85
Figure 88.	+45° Repair Individual Rivet Model Mode 1, $f = 488$ hz	87
Figure 89.	+45° Repair Perfect Bond Model Mode 1, $f = 559$ hz . .	87
Figure 90.	+45° Repair Individual Rivet Model Mode 2, $f = 510$ hz	88
Figure 91.	+45° Repair Perfect Bond Model Mode 2, $f = 583$ hz . .	88
Figure 92.	+45° Repair Individual Rivet Model Mode 3, $f = 737$ hz	89
Figure 93.	+45° Repair Perfect Bond Model Mode 3, $f = 783$ hz . .	89
Figure 94.	+45° Repair Individual Rivet Model Mode 4, $f = 799$ hz	90
Figure 95.	+45° Repair Perfect Bond Model Mode 4, $f = 886$ hz . .	90
Figure 96.	+45° Repair Individual Rivet Model Mode 5, $f = 854$ hz	91
Figure 97.	+45° Repair Perfect Bond Model Mode 5, $f = 917$ hz . .	91
Figure 98.	+45° Repair Effects	92
Figure 99.	-45° Repair Individual Rivet Model Mode 1, $f = 476$ hz .	94
Figure 100.	-45° Repair Perfect Bond Model Mode 1, $f = 608$ hz . .	94
Figure 101.	-45° Repair Individual Rivet Model Mode 2, $f = 513$. .	95
Figure 102.	-45° Repair Perfect Bond Model Mode 2, $f = 642$ hz . . .	95
Figure 103.	-45° Repair Individual Rivet Model Mode 3, $f = 702$. .	96
Figure 104.	-45° Repair Perfect Bond Model Mode 3, $f = 831$ hz . .	96
Figure 105.	-45° Repair Individual Rivet Model Mode 4, $f = 775$	97
Figure 106.	-45° Repair Perfect Bond Model Mode 4, $f = 943$ hz . .	97
Figure 107.	-45° Repair Individual Rivet Model Mode 5, $f = 842$ h . .	98

Figure 108. -45° Repair Perfect Bond Model Mode 5, $f = 948$ hz . . .	98
Figure 109. -45° Repair Effects	99

List of Tables

Table Name	Page Number
Table 1. AS4/3501 Material Properties	25
Table 2. Refinement Results	27
Table 3. Patch Material Properties	31
Table 4. Equivalent Laminate Material Properties	33
Table 5. Overlap Material Properties	33
Table 6. Full Panel Results	38
Table 7. 0° Cutout Section Model Results	44
Table 8. 90° Cutout Section Model Results	49
Table 9. +45° Cutout Section Model Results	57
Table 10. -45° Cutout Section Model Results	62
Table 11. 0° Repair Model Results	68
Table 12. 90° Repair Model Results	79
Table 13. +45° Repair Model Results	86
Table 14. -45° Repair Model Results	93

ABSTRACT

△ To analyze the current Aircraft Battle Damage Repair (ABDR) techniques, a finite element model (FEM) of a curved composite panel with a center cutout section was developed and verified against previously obtained modal test results. The FEM was modified using different methods to exhibit the effects of riveting on an aluminum patch to repair the section. The different methods were contrasted against each other and previously obtained modal test results.

The panel, a $[0/-45/+45/90]$, layup of AS4/3501 graphite epoxy measuring 12" in height and 12.19" across its arc length with a 2" by 4" cutout at a 0, +45, -45, or 90 degree orientation was modeled using MSC/NASTRAN QUAD4 elements. The first repair modeling method used a mixture of the aluminum and composite panel properties to represent the overlap region of the patch. The second method used ELAS2 and CONM2 elements to model the rivets, and modeled the panel and the patch separately. GAP elements prevented the patch from deforming through the panel.

For the mixed properties, the mode shapes agreed with experimental data at lower frequencies but were distorted at the higher ones and were regularly 5-25% high. Modeling the rivets individually produced matching mode shapes and frequencies regularly within 5% of experimental values. ←

FINITE ELEMENT MODELING OF A RIVETED PATCH ON A COMPOSITE PANEL

I INTRODUCTION

The many advantages of the material properties afforded by today's advanced composite materials have brought about their wide use in the manufacture of many of today's aerospace vehicles. But the application of composites to existing structural problems is a young science, and not a fully explored one. Particularly in military aircraft, the behavior of damaged composites and subsequent repairs are of great interest.

The current Aircraft Battle Damage Repair (ABDR) techniques for the repair of battle damaged composite panels, based on simplicity, speed, and reliability of the repair, require that an aluminum patch be fastened with bolts over the damaged section of the composite panel. The purpose of ABDR is not to fully restore the original properties of the panel. It is instead intended to match the properties closely enough that the aircraft can be returned to service in a timely manner or, if damaged beyond the repair abilities of the unit, allow the aircraft to safely fly to a more capable repair facility [18:1].

The static analysis of such repairs has been well researched, including the development of the McDonnell Douglas CREPAIR program for static analysis of mechanically fastened repairs to composite shells [9:11]. However, the dynamic analysis of a mechanically fastened repair is a relatively unexamined though important problem.

Understanding of how these repairs might affect the natural frequencies of the panel is essential. The natural frequency is the frequency that a lightly damped structure can vibrate at a continually increasing amplitude [20:86]. To avoid a failure of the section under otherwise normal operating condition, the effect of the repair on the natural frequency should be ascertained. This provides a complicated problem for analysis: determining the dynamic behavior for a curved panel with a convoluted geometry and complicated material properties. Although closed-form solutions exist for many simpler geometries, the combination of unusual geometric boundary conditions and complicated material analysis of composite shell properties present great difficulties [15:205]. This problem, however, is suitable for a finite element oriented solution.

BACKGROUND

In 1985, Walley [23] investigated the effects of the size of an interior cutout section on the modal behavior of a curved rectangular composite panel using both interferometric holographic techniques and the

finite element code STAGS C-1. In 1986, Cyr [5] followed this effort by investigating the effects of orientation of a 2" by 4" interior cutout section on the modal behavior of a curved rectangular composite panel using interferometric holography techniques and the finite element code STAGS C-1. In 1988, Goodwin [7] analyzed the effect of riveting an aluminum patch to a curved rectangular composite panel over a 2" by 4" interior cutout section at different orientations using interferometric holography techniques and the finite element code NISA. Goodwin was limited by the capabilities of the PC-based NISA code, and therefore could only model the symmetric cases and modeled the repair by assuming that the patch was perfectly bonded to the panel. The perfect bond assumption means that the panel and patch maintain the identical deformation at all locations where they overlap. In 1989, Levraea [12] investigated the the effects of eccentrically located cutout sections on the modal behavior of a curved rectangular composite panel subject to a free-clamped-free-clamped boundary condition using video holography and STAGS-C1.

As a direct precursor to the attempt to model the individual rivets for this thesis, also in 1988, a paper by Henriquez, McLaughlin, Montgomery, and Ruggerio [8] discussed the study of modeling of various thin interfaces typically encountered in small resonant structures, including two surfaces bolted together. Two free, circular, aluminum plates were connected with six bolts which were modeled by spring elements and concentrated mass

elements. However, the analytical model seemed to indicate that the two plates were not coupled since the resonant frequency was similar to that of an individual plate was obtained [8:430]. The authors did not attempt to explain why this might have occurred.

METHODOLOGY

In order to compare to Goodwin's experimental results and to avoid a duplication of his efforts, the curved rectangular composite panel used in this thesis is identical to the one described in Goodwin [7:3.1-3.1]. Similarly, the patch and the fasteners are modeled on those used by Goodwin [7:3.5,3.10].

Although the STAGS C-1 analysis was based on the Kirchhoff-Love hypothesis and neglected transverse shear while the NISA analysis included it by using Reissner-Mindlin theory, both codes used shell elements with higher-order shape functions to model the curved panel [6:2.22]. This investigation used MSC/NASTRAN QUAD4 elements that combine bending and extensional behavior into a single 2-D isoparametric element that includes transverse shear effects. The curved panel was then modeled using a sufficient number of flat plate elements so that the curvature across each individual element was negligible. This allowed the use of simpler plate elements, as well as a simpler plate analysis of the properties of the composite laminate. The QUAD4 elements use a simpler shape function

than the NKTP 32 shell elements used by Goodwin, and provide for easier computational solutions. The properties of a composite plate are dependent upon the curvature of the mid-surface of the plate, and a composite shell has a pre-existing curvature of the midsurface prior to deformation which greatly increases the complexity of the governing equations.

As a basis for comparison to Goodwin's results, the repair was modeled using elements with a blend of the properties of the composite panel and aluminum patch, including the mass of the rivets, in the region of the panel where the patch overlaps the panel in order to simulate a perfect bond between the patch and the panel. The main effort of this thesis was to more accurately model the effects of the patch, so the patch and panel were modeled as separate entities, and the individual rivets were individually modeled to connect the two curved surfaces.

MSC/NASTRAN ELAS2 spring elements were used to model the stiffness contribution of the rivets, and CONM2 concentrated mass elements were used to represent the mass of each rivet. GAP elements, nonlinear elements intended for use with nonlinear geometries, were used to maintain the proper spacing between the midsurfaces of the panel and the patch. MSC/NASTRAN SINV (Sturm Inverse Power Method) was used to solve the resulting eigenvalue problem.

SDRC I-DEAS was used to generate the geometry of the models, define the physical properties of the elements, write the MCS/NASTRAN

data deck, and to graphically represent the mode shapes resulting from the MSC/NASTRAN analysis.

A Sun4 workstation was used to run the programs necessary for the execution of this thesis. SDRC I-DEAS Level V was used for the pre- and post-processing, and MSC/NASTRAN v66 was used to perform the analysis.

II THEORY

OVERVIEW

This section covers the three theories that enabled the completion of this analysis: Laminated Plate Theory (LPT), the Finite Element Method (FEM) and the Sturm inverse power eigenvalue solution technique. LPT allows a ply-by-ply compilation of the properties of a laminated composite to develop the material properties of the laminate. Using FEM, these material properties can be used to build a mathematical model of the curved panel. The dynamic behavior of the model can be determined by application of an appropriate solution technique to the eigenvalue problem. For this thesis, since a limited number of eigenvalues was sought within a known range, the Sturm inverse power method was used.

LAMINATED PLATE THEORY (LPT)

LPT assumes, for simplification of analysis, that a perfect bond exists between each lamina, that each lamina can be considered to be in a state of plane stress, and that displacement is continuous in the z-direction [20:51]. LPT combines the macromechanical analysis of individual laminae with these three assumptions to describe the layup as a whole. This analysis is briefly covered here to show the inclusion of transverse shear stress as used by MSC/NASTRAN [20:2.12-1 to 2.12-13].

The stress is related to strain in QUAD4 elements by the relationship

$$\begin{Bmatrix} f \\ m \\ q \end{Bmatrix} = \begin{bmatrix} G_1 & G_4 & 0 \\ G_4 & G_2 & 0 \\ 0 & 0 & t_e G_3 \end{bmatrix} \begin{Bmatrix} \epsilon_m \\ \chi \\ \gamma \end{Bmatrix} \quad (1)$$

where $\{f\} = [f_x, f_y, f_{xy}]^T$, the membrane forces/unit length;
 $\{m\} = [m_x, m_y, m_{xy}]^T$, the bending moments/unit length; $\{q\} = [q_x, q_y]^T$, the transverse shear force/unit length; $\{\epsilon\} = [\epsilon_x, \epsilon_y, \epsilon_{xy}]^T$, the membrane strains at the laminate center; $\{\chi\} = [\chi_x, \chi_y, \chi_{xy}]^T$, the curvatures; and $\{\gamma\} = [\gamma_x, \gamma_y]^T$, the transverse shear strains. t_e is the effective thickness for transverse shear such that ($t_e = t \cdot 5/6$) to account for the parabolic distribution of shear stresses through a laminate of thickness t . This neglects thermal effects.

For a laminate with N -plies of constant thickness, the terms $[G_1]$, $[G_2]$ and $[G_4]$ are defined by

$$[G_1] = \sum_{k=1}^N \int_{-\frac{1}{2} + \frac{(k-1)t}{N}}^{-\frac{1}{2} + \frac{kt}{N}} [G_0]_k dz \quad (2)$$

$$[G_2] = \sum_{k=1}^N \int_{-\frac{1}{2} + \frac{(k-1)t}{N}}^{-\frac{1}{2} + \frac{kt}{N}} [G_0]_k z^2 dz \quad (3)$$

$$[G_d] = \sum_{k=1}^N \int_{-\frac{t}{2} + \frac{(k-1)t}{N}}^{-\frac{t}{2} + \frac{kt}{N}} [G_e]_k(-z) dz \quad (4)$$

where the $[G_e]$ for orthotropic materials is

$$[G_e] = \begin{bmatrix} \frac{E_1}{1-\nu_1\nu_2} & \frac{\nu_1 E_2}{1-\nu_1\nu_2} & 0 \\ \frac{\nu_2 E_1}{1-\nu_1\nu_2} & \frac{E_2}{1-\nu_1\nu_2} & 0 \\ 0 & 0 & G_{12} \end{bmatrix} \quad (5)$$

and is composed of the material properties of the specific lamina in the material axis system. The material axis system is transformed to the elemental axes by

$$[G_d] = [T]^T [G_e] [T] \quad (6)$$

where

$$[T] = \begin{bmatrix} \cos^2\theta & \sin^2\theta & \cos\theta\sin\theta \\ \sin^2\theta & \cos^2\theta & -\cos\theta\sin\theta \\ -2\cos\theta\sin\theta & 2\cos\theta\sin\theta & \cos^2\theta - \sin^2\theta \end{bmatrix} \quad (7)$$

The $[G_s]_m$ matrix of transverse shear moduli is defined by

$$[G_3]_m = \begin{bmatrix} G_{11} & G_{12} \\ G_{21} & G_{22} \end{bmatrix} \quad (8)$$

which is transformed to the element coordinate system by

$$[G_3]_e = [W]^T [G_3]_m [W] \quad (9)$$

where

$$[W] = \begin{bmatrix} \cos\theta & \sin\theta \\ -\sin\theta & \cos\theta \end{bmatrix} \quad (10)$$

The value of the transverse shear modulus for the entire laminate is derived from the transverse shear strain energy such that the 2×2 matrix is defined by

$$\bar{G}_m = \left[\frac{T}{\bar{E}_{11}^2} \sum_{k=1}^N [G_{1m}^k]^{-1} R_{1k} \right] \quad (11)$$

where \bar{E}_{11} and \bar{E}_{22} are the 1,1 and 2,2 terms of $[G_2]^*$ respectively when $[G_2]^*$ is the same as $[G_2]$ when $\nu = 0$ and

$$R_{1k} = \left\{ \frac{1}{3} (\bar{z}_1 - 2z_{k-1}) - \frac{1}{4} t_k \right\} \bar{z}_1 t_k^2 + \left\{ \frac{1}{3} z_{k-1}^2 + \frac{1}{4} z_{k-1} t_k + \frac{1}{20} t_k^2 \right\} t_k^2 \quad (12)$$

FINITE ELEMENT METHOD (FEM)

FEM takes a complicated problem and divides it into many smaller problems that are more readily solvable [17:1]. Whereas the dynamic analysis of a fully clamped, rectangular, curved composite panel is difficult to obtain analytically, the solution for a similar simply supported flat plate is well known [22:87]. Similarly, developing the stiffness matrices for a curved composite shell is more involved than the flat plate condition due to the initial curvature of the midsurface. However, all this means that the solution provided by the FEM is only an approximation of the exact solution, and is not exact. It can be shown to converge on the exact solution, given enough iterations and providing that compatibility relationships are satisfied [3:126].

This section is not meant as a thorough development of Finite Element Analysis (FEA); rather, it is intended to highlight those portions of the theory important to this thesis. First, the general methods and requirements of displacement based FEA will be briefly reviewed. Then the abilities and limitations of the particular MSC/NASTRAN elements used will be covered in the section most applicable.

FEA TENETS. The first step in the creation of a finite element model is to discretize the subject [17:8]. For this project, that consisted of dividing the curved composite panel into flat elements and determining the best method to represent the effects of the rivets. Only the displacement

(translational and rotational) at the corners or ends (nodes), of the elements are affected by the displacement functions. They are related to each other by interpolation formulae, and it is these formulae that define the shape and abilities of the element. These shape functions are arranged into a matrix $[N]$, and can then be used to formulate the stiffness matrix for the element. First, the continuous displacement field $\{u\}$ is related to the interpolation of the discretized displacements $\{d\}$ by

$$\{u\} = [N]\{d\} \quad (13)$$

Now, the discretized displacement can be related to the elemental strains in much the same manner that continuous displacement fields: by differentiation. The equation

$$\{e\} = [\partial]\{u\} \quad (14)$$

for a set of continuous displacements yields

$$\{e\} = [B]\{d\} \quad (15)$$

for a set of discretized displacements where

$$[B] = [\partial][N] \quad (16)$$

The $[\partial]$ matrix is dependent on strain-displacement relationships specific to the problem being modeled.

As can be found in almost any finite element text (see [3:110] or [13:85-86]), the elemental stiffness matrix $[k]$ can be derived from the principle of minimum potential energy, resulting in the volume integral

$$[k] = \int_V [B]^T [E] [B] dV \quad (17)$$

where $[E]$ is the matrix comprised of the stress-strain relationships for the discretized system, much as the $[B]$ matrix is comprised of the strain-displacement relationships. For this thesis, $[E]$ is the stress-strain relationship defined in Equation 1.

It is important to note that the $[E]$ and $[B]$ matrices determine how fully the actual physical system is represented in the finite element model. For this thesis, a full, three-dimensional model was not created. Rather, the panel was modeled using idealized two-dimensional plate elements which are considered to be in a state of plane stress. Similarly, the full three-dimensional effects of the rivets were not modeled; they were represented by spring elements that only considered one-dimensional effects. These simplifications streamlined the modeling process, but still resulted in an accurate solution.

Since every differential element of a continuum can be considered to be in static equilibrium and compatibility prevails everywhere, a finite element model should attempt to reasonably simulate this. As stated in

Cook, the extent to which equilibrium and compatibility conditions can be satisfied are:

1. Equilibrium of nodal forces and moments is satisfied.
2. Compatibility prevails at nodes.
3. Equilibrium is usually not satisfied across interelement boundaries.
4. Compatibility may or may not be satisfied across interelement boundaries.
5. Equilibrium is usually not satisfied within elements.
6. Compatibility is satisfied within elements.

[124-126]

Simply stated, these mean that compatibility and equilibrium must be satisfied between nodes, although they needn't necessarily be satisfied between elements. However, the incompatibilities across element borders should tend toward zero as more elements are used. This is important when the use of flat elements to model a curved panel is considered. Modeling a shell with plate elements provides for an incompatibility in the elemental out-of-plane rotations, as is depicted in Figure 1. Because the elemental

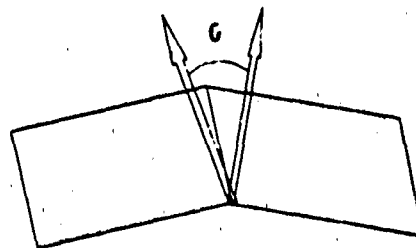


Figure 1.
Z-axis Rotation Incompatibility

z-axes differ by the small angle θ , neither rotation can be maintained since

the element has no stiffness in that direction [14:181]. MSC/NASTRAN automatically restrains this so called "drilling" degree of freedom in order to eliminate this incompatibility, which tends to artificially stiffen any model using elements oriented in such a manner. Increasing the number of elements should, however, decrease this effect.

In order to accomplish a dynamic analysis using the finite element method, not only must the stiffness of the model be represented mathematically, the mass of the model also must be expressed in matrix form. Two different methods are available to accomplish this in MSC/NASTRAN, the lumped-mass matrix and the consistent mass matrix.

The lumped mass method simply apportions the mass of the element equally among the translational degrees of freedom. This assumes that the material within the mean location on either side of the particular displacement behaves like a rigid body while the rest of the element does not participate in the motion. Because this excludes the dynamic coupling that exists between the element displacements, it has the advantage of creating a diagonal matrix; but, it usually ignores the effects of rotary inertia [17:365]. For most dynamic cases where the displacements are small, the effects of rotary inertia are not notable, so neglecting them should not be a cause for error.

The consistent mass matrix is defined by the volume integral

$$[m] = \int_V [N]^T \rho [N] dV \quad (18)$$

where ρ is the density of the element and $[N]$ is the shape function. Since the consistent mass matrix depends on the shape function, it will generally be a fully populated matrix [13:475]. The consistent mass matrix automatically includes the rotary inertia terms, and the off-diagonal terms represent the dynamic coupling terms. This method involves an integral, which must be approximated for use on a computer, and is therefore more numerically complex than the lumped mass matrix approach, and requires more computer storage space. Also, the diagonal lumped mass matrix can facilitate the computational procedures [17:365]. For this thesis, though, the results differed by less than 1% depending on the mass matrix used. Since the lumped mass matrix provided for a faster solution, it was applied to all the model solutions for this project.

QUAD4 ELEMENT. The MSC/NASTRAN QUAD4 element was developed using a four-noded isoparametric formulation so that it could be used for an arbitrary quadrilateral geometry. Its development is well documented and only the highlights are presented here [14:175]. The element was developed for use with anisotropic properties, and features an elastic coupling between bending and stretching and an augmentation of transverse shear flexibility. To do this requires modifying the standard

isoparametric theory for both membrane and bending action.

The first change involves computing the shear strain γ_{xy} at the center of the element ($\xi = \eta = 0$). This value is used to evaluate stresses and strain energy at a 2×2 array of Gauss points, together with strains ϵ_x and ϵ_y , computed directly at these points [14:177]. This is a modification to the standard isoparametric theory for membrane action, and permits element edges to be curved.

To modify the bending action, the out-of-plane displacements are now defined as a double power series in ξ and η :

$$w = w_{00} + w_{10}\xi + w_{01}\eta + w_{20}\xi^2 + w_{02}\eta^2 + w_{11}\xi\eta + \dots \quad (19)$$

If the coefficients are arranged in a pyramid as shown in Figure 2,

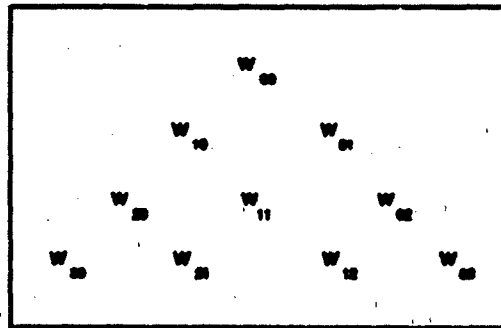


Figure 2
Coefficient Triangle

then the first two rows represent the rigid body motions and constant transverse shear strains, the third row represents the constant curvatures, and the fourth row represents curvatures that vary linearly with ξ and η .

The w_{20} and w_{02} terms require reduced order integration of the energy due to the transverse shear, and the w_{30} and w_{03} terms can be corrected by the introduction of residual bending flexibility. This is done by setting the conditions for curvature dependence to be the curvature compatibility conditions for a plate with zero transverse shear strains,

$$\left. \begin{aligned} \frac{\partial \chi_{xy}}{\partial x} &= 2 \frac{\partial \chi_x}{\partial y} \\ \frac{\partial \chi_{xy}}{\partial y} &= 2 \frac{\partial \chi_y}{\partial x} \end{aligned} \right\} \quad (20)$$

which are satisfied if the twist used compute the strain energy is

$$\bar{\chi}_{xy}^g = 2\chi_{xy}^g - \chi_{xy}^0 \quad (21)$$

where χ_{xy}^g is the value of twist computed at any integration point g and χ_{xy}^0 is the value of twist computed at $\xi = \eta = 0$. Thus the energy due to bending is computed by a numerical integration at a 2×2 array of Gauss points. However, this leads to an energy deficiency. It is correctable, though, by the introduction of residual bending flexibility.

ELAS2 ELEMENT. The ELAS2 element (shown in Figure 3) is simply a three-dimensional translation spring element. It can act as up to three independent translational springs acting along three orthogonal directions, with each direction having its own spring stiffness constant. Its

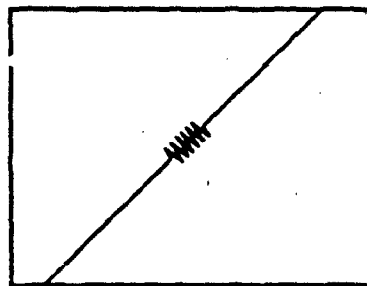


Figure 3.
ELAS2 Element

stiffness matrix is simply defined by

$$f_i = K_i x_i \quad (22)$$

where K_i is the directional stiffness, x_i is the directional displacement, and f_i is the force acting on it. It was used in this project to simulate the stiffness of the rivets by equating each K_i with Young's Modulus of Elasticity of aluminum.

GAP ELEMENT. The GAP element (shown in Figure 4) has a

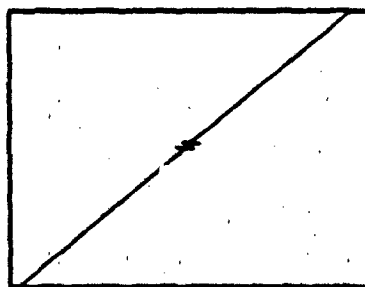


Figure 4.
GAP Element

conditional stiffness matrix. With the definition of an initial gap opening, the GAP element will exhibit different values of axial stiffness, depending

on whether the initial separation distance has increased or decreased. It can also provide for transverse stiffness when the gap separation is open (separation greater than initially defined), as well as coefficients of friction in transverse directions. These latter capabilities were not explored in this thesis, as no transverse motion was expected. The GAP element was used to maintain the initial separation between the midsurfaces of the panel and the patch. This will be more fully explained in the next chapter.

EIGENVALUE ANALYSIS

From Newton's Second Law, the following equation governs motion for a discretized system [21:144]:

$$[M]\{\ddot{x}\} + [C]\{\dot{x}\} + [K]\{x\} = \{F(t)\} \quad (23)$$

where $[M]$ is the mass matrix, $[C]$ is the damping matrix, $[K]$ is the stiffness matrix, $\{x\}$ is the position, and $\{F(t)\}$ is the external forces acting on the system. For the free vibration of a thin plate where damping can be considered negligible, $[C] = 0$ and $\{F(t)\} = 0$. Now the governing equation is

$$[M]\{\ddot{x}\} + [K]\{x\} = \{0\} \quad (24)$$

By assuming a displacement function of the form

$$\{x\} = \{\phi\}e^{i\omega t} \quad (25)$$

and substituting into Equation (24), the characteristic eigenvalue problem is derived:

$$[K] - \omega^2[M]\{\phi\} = 0 \quad (26)$$

for which non-trivial solutions exist only when

$$|[K] - \omega^2[M]| = 0 \quad (27)$$

The Sturm Inverse Power Method (SINV), which is a variant of the inverse power method, was used to solve for the eigenvalue $\lambda = \omega^2$ using shifts for faster convergence, sweeping to eliminate effects of prior eigenvalues, and the application of Sturm sequence polynomials to aid the control of the iteration process [20:4.4-40].

Shifting the solution algorithm to an initial Λ_0 such that

$$\lambda = \lambda_0 + \Lambda \quad (28)$$

so Λ replaces λ as the eigenvalue parameter, producing

$$[K - \lambda_0 M]\{\phi\} = \Lambda[M]\{\phi\} \quad (29)$$

which is the basis of the iteration scheme

$$[K - \lambda_0 M]\{\phi_n\} = [M]\{u_{n-1}\} \quad (30)$$

$$\{u_n\} = \frac{1}{C_n} \{\phi_n\} \quad (31)$$

[20:4.4-24]

where C_n is equal to the element of $\{\phi\}$ with the greatest absolute value and $1/C_n$ converges to Λ_1 , the shifted eigenvalue nearest the shift point, and $\{u_n\}$ converges to the corresponding eigenvector.

This eigenvector can be eliminated via a sweeping procedure, since all the eigenvectors are orthogonal [15:119]. For a discretized system, the number of degrees of freedom equals the number of eigenvalue solutions to Equation (27) [17:153]. Therefore, once the first eigenvalue has been found, the size of characteristic equation can be reduced to accelerated to determination of the next eigenvalue.

To solve Equation (30), the SINV solution method decomposes the $[K - \lambda_0 M]$ matrix into triangular factors such that

$$[K - \lambda_0 M] = [L][D][L]^T \quad (32)$$

where $[L]$ is a lower triangular matrix with ones on its diagonal and $[D]$ is a diagonal matrix consisting of the terms on the diagonal of the $[K - \lambda_0 M]$ matrix. Then the characteristic polynomials of the leading principal submatrix of the $[K - \lambda_0 M]$ matrix can be written as a Sturm sequence of

polynomials. It can then be shown that the number of sign agreements in the Sturm sequence corresponds to the number of negative values in the diagonal [D] matrix, which equals the number of eigenvalues of $[K - \lambda_0 M]$ below λ_0 [20:4.4-34]. This is calculated for each shift, and is used in the control of the iteration process.

III FINITE ELEMENT MODELING

In order to validate this analysis, three steps were necessary. First the properties of the [0/-45/+45/90], AS4/3501 Hercules graphite epoxy needed to be modeled. Then a model of the full undamaged panel needed to be created and solved, and the results compared to the experimental data of Goodwin. Finally, four more models were necessary, one for each of the following cutout section orientations: 0°, 90°, +45°, and -45°. The results from these analyses were then compared to the experimental results of Goodwin.

Once the validation of the panel modeling was complete, the cutout section models were changed by adding an aluminum patch over the cutout section. This was done by two methods. The first assumed that the patch was perfectly bonded to the panel. The other method modeled the rivets individually.

LAMINATE PROPERTY MODELING

The orthotropic material properties used by Goodwin, listed in Table 1, were used to create an orthotropic material table in SDRC I-DEAS. Using the Laminate Modeling Task to define the orientation and thickness of each ply allowed SDRC I-DEAS to calculate the laminate

Table 1. AS4/3501 Material Properties

Material Property		Value
Modulus of Elasticity	E_1	18.84e6 psi
	E_2	1.468e6 psi
Shear Modulus	G_{12}	0.9099e6 psi
	G_{23}	0.9099e6 psi
	G_{13}	0.7279e6 psi
Poisson's Ratio	ν_{12}	0.2799
	ν_{21}	0.0218
Density	ρ	1.516e-4*
Thickness	t	0.005"

(* units for ρ are $\text{lb}_f \cdot \text{s}^2/\text{in}^4$)

properties which are displayed graphically in Figure 5. These material properties were then oriented on all panel elements so that the primary element material axis was parallel to the global z-axis.

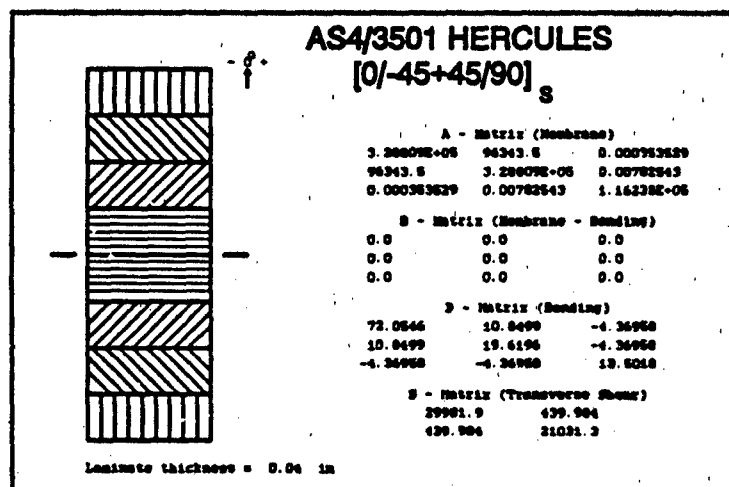


Figure 5. Laminate Properties

FULL PANEL MODEL

The full panel was modeled first by using elements approximately $\frac{1}{2}$ " square ($0.500" \times 0.508"$) as is shown in Figure 6. The outer

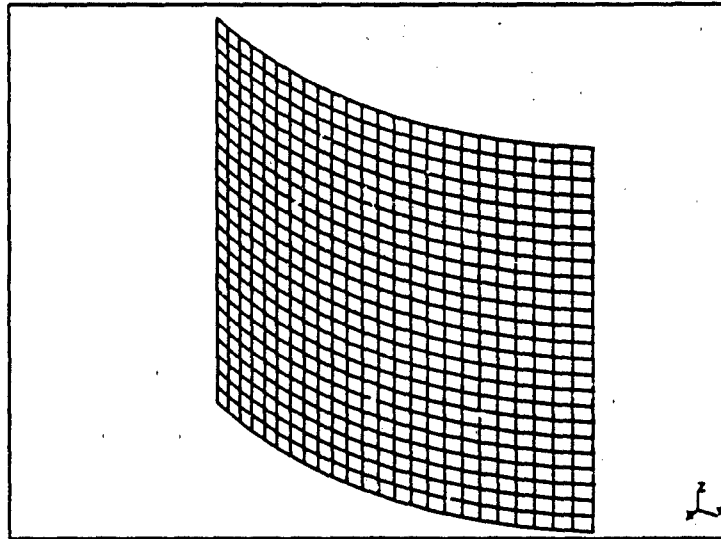


Figure 6. Full Panel Model

dimensions ($12"$ high by $12.19"$ arc length across a $12"$ radius of curvature) are the same for all the models, and the same as those used in experiments of Goodwin, Cyr, and Walley.

To insure that the model would converge, the mesh was refined so that the elements were approximately $\frac{1}{4}"$ square ($0.250" \times 0.254"$) as is shown in Figure 7. These results were contrasted against the frequency

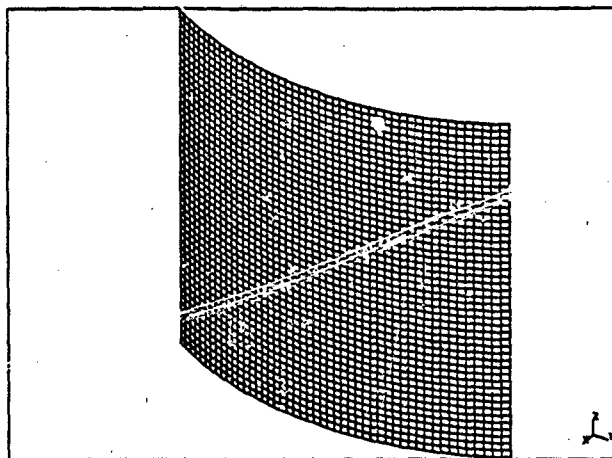


Figure 7. Refined Panel Model

results for the first five modes of the previous model and the experimental data, as well as the cpu time required to compute the solution in order to determine the optimal modeling option (see Table 2). On this basis, it was

Table 2. Refinement Results

Source	f_1	f_2	f_3	f_4	f_5	cpu (s)
½" Mesh	558	591	761	825	916	3359.3
¼" Mesh	550	571	755	820	905	15918.3
Goodwin Exper.	514	519	716	727	821	N/A

(* All frequencies in hertz)

decided to use the first (coarser) mesh as a basis for construction of the other models, as the increase in accuracy was severely outweighed by the increase in computational effort.

CUTOUT SECTIONS

0° AND 90° SECTIONS. These models, shown in Figure 8 and Figure 9, were very similar to the full panel model since the cutout sections

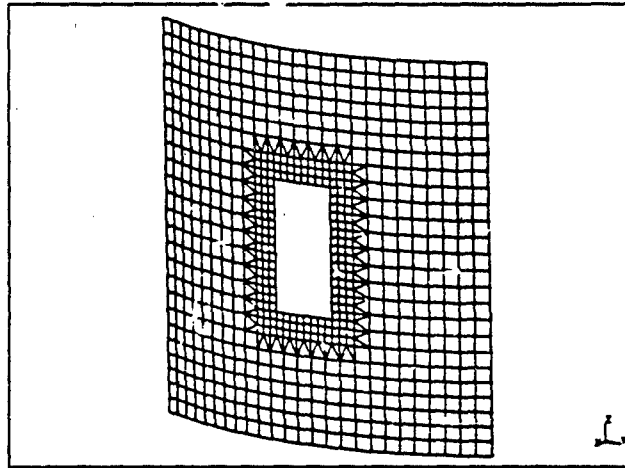


Figure 8. 0° Cutout Section Model

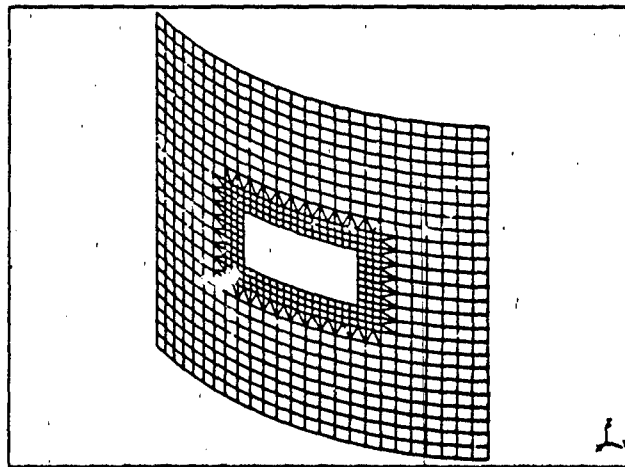


Figure 9. 90° Cutout Section Model

for both of these models were aligned with the element orientation.

However, in order to create a geometry capable of supporting nodes at the locations that will be used to model the riveted connections, the mesh

needed to be refined within 0.75" of the cutout, to a 0.25" \times 0.25" grid. Triangular TRIA3 elements were used to transition from the outer to the inner grid. Although MSC/NASTRAN advocates the use of RSPLINE elements for this task, doing so would disallow the use of SDRC I-DEAS as a post-processor, since that element is not supported by I-DEAS Level V.

***45° SECTIONS.** Since the mode shapes of a cylindrical section tend to be aligned with the global z-axis of the panel, these models presented a set of contradictory demands: the elements should be aligned with cutout section for the most physically accurate model, yet the elements should be aligned with the expected mode shapes so that the interpolation functions are best able to approximate the actual displacement function. Initial attempts to align the elements with the cutout were unsuccessful, as the mode shapes were deformed and in some cases unrecognizable. Using a 34 \times 34 alleviated this problem, though. Its elements were 0.353" \times 0.359" with a diagonal measuring 0.503". Thus, a cutout section measuring 3.95" \times 1.97" was created, and the elements were aligned with the expected displacement functions. These models are shown in Figure 10 and Figure 11.

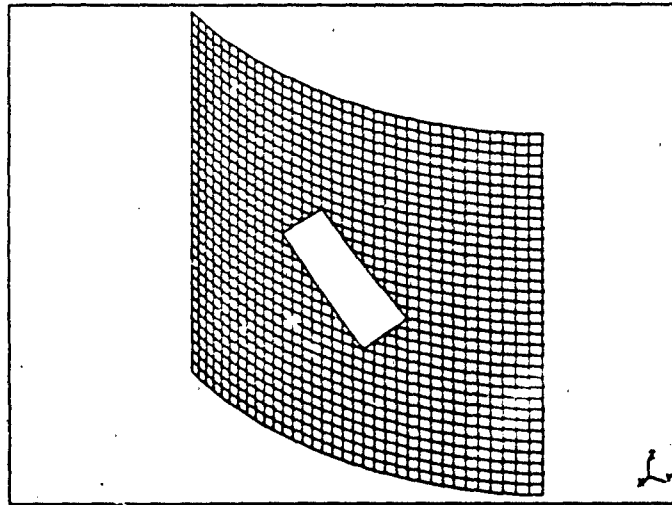


Figure 10. +45° Cutout Section Model

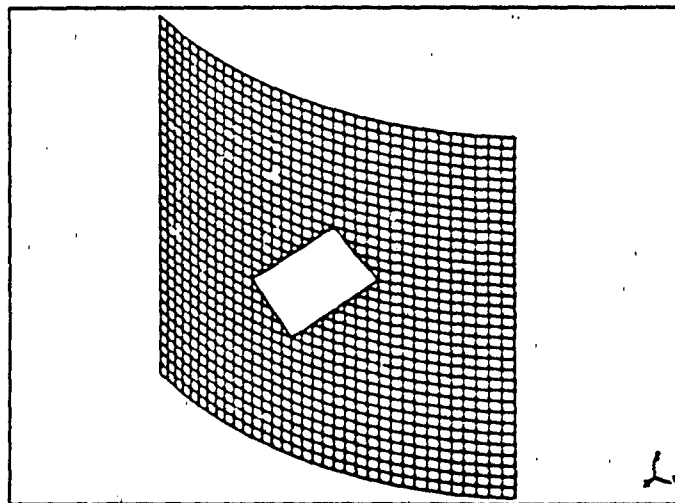


Figure 11. -45° Cutout Section Model

The presence of triangular elements along the border of the cutout sections should not present any difficulties in achieving an accurate solution, since the cutout section will not create the type and magnitude of stress concentrations in a dynamic analysis as it would in a static loading analysis.

PATCH MODELING

PERFECT BOND MODEL. Assuming that the patch is perfectly bonded to the panel has been the standard assumption in prior attempts to model the dynamic behavior of a repaired panel. This was done in this project to provide a baseline for comparison to the individual rivet modeling method. To prepare this model, the mesh was divided into three regions: the panel, the patch, and the overlap (see Figure 12). The panel's characteristics were unchanged from the cutout model, and the patch was modeled using the isotropic aluminum properties shown in Table 3. The

Table 3. Patch Material Properties

Material Property		Value
Modulus of Elasticity	E	10.5e6 psi
Poisson's Ratio	ν	0.33
Density	ρ	2.617e-4*
Thickness	t	0.032"

(* units for ρ are $\text{lb}_f \cdot \text{s}^2/\text{in}^4$)

overlap region was modeled using a mixture of the aluminum and laminate properties, which were calculated using a method similar to the rule of mixtures used to determine the properties of a composite based on the fiber/matrix volume ratio. In order to be able to do this, equivalent transverse isotropic properties were needed for the laminate. Since the layup is balanced and symmetric, the following equations apply:

$$E_x = \frac{(A_{11}A_{22} - A_{12}^2)}{tA_{22}} \quad (33)$$

$$E_y = \frac{(A_{11}A_{22} - A_{12}^2)}{tA_{11}} \quad (34)$$

$$\nu_{xy} = \frac{A_{12}}{A_{22}} \quad (35)$$

$$\nu_{yx} = \frac{A_{12}}{A_{11}} \quad (36)$$

$$G_{xy} = \frac{A_{66}}{t} \quad (37)$$

where A_{ij} is defined by

[2:34]

$$A_{ij} = \sum_{k=1}^N (\bar{Q}_{ij})_k (z_k - z_{k-1}) \quad (38)$$

and \bar{Q}_{ij} is the transformed reduced stiffness matrix for a given ply, and the distance from the midsurface to the bottom of the k^{th} ply is z_k . The resulting properties can be found in Table 4.

Table 4. Equivalent Laminate Material Properties

Material Property		Value
Modulus of Elasticity	E_x	7.515e6 psi
	E_y	7.515e6 psi
Poisson's Ratio	ν_{xy}	0.293
	ν_{yx}	0.293
Shear Modulus	G_{xy}	2.906e6 psi

The resulting material properties for the overlap section can be found in Table 5.

Table 5. Overlap Material Properties

Perfectly Bonded Patch/Panel Material		
Material Property		Value
Modulus of Elasticity	E	8.8e6 psi
Poisson's Ratio	ν	0.309
Density	ρ	2.018e-4*

(* units for ρ are $\text{lb}_f \cdot \text{s}^2/\text{in}^4$)

RIVET MODELING. The ABDR requirements dictated the size of patch and the placement of the rivets (see Figure 12). The patch was generated as a refined $\frac{1}{4}$ " square $3.5" \times 5.5"$ mesh $0.036"$ above the panel, the distance from the midsurface of the panel to the midsurface of the patch. Spring elements, lumped mass elements, and gap elements were

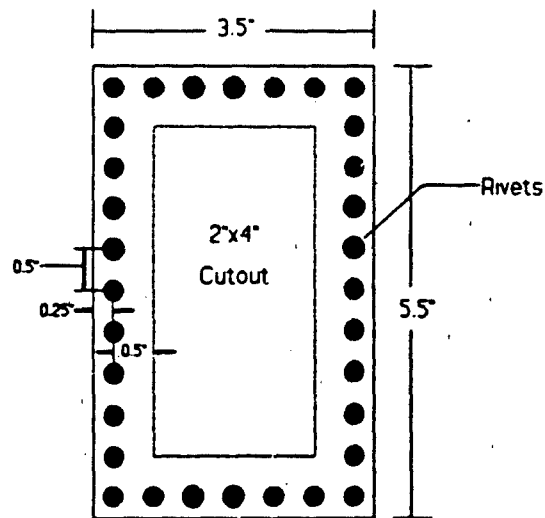


Figure 12. Rivet Placement

used to model the rivets and separation, as can be seen in Figure 13.

Node-to-node translational spring elements were generated at the rivet locations in SDRC I-DEAS, which translated into ELAS2 elements in MSC/NASTRAN. SDRC I-DEAS lumped mass elements, which became CONM2 MSC/NASTRAN elements, were generated at both end nodes, each representing half of the rivet mass ($2.139\text{e-}6 \text{ lb}_f \cdot \text{s}^2/\text{in}$). SDRC I-DEAS gap elements, equivalent to MSC/NASTRAN GAP elements, were applied to the nodes on the edge of the cutout section of the panel and the outer edge of the patch, and the opposing nodes of the opposite surface. The nodes between the edges did not have gap elements separating the two surfaces since this was found to over-constrain the model and prevent solution. However, the separation of these inner nodes did not vary in any appreciable manner, due largely to the inherent stiffness of the elements.

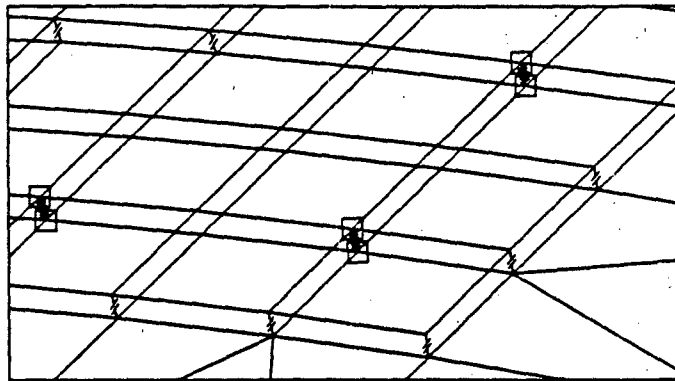


Figure 13. Close View of Patch

In Figure 13, the bottom layer of quadrilateral elements is the composite panel, and the top layer of quadrilateral elements is the aluminum patch. The lumped mass elements are represented by squares around their nodal locations, and the spring elements show the rivet placement and modeling. Along the outer edge of the patch are the GAP elements, as well as along the edge of the cutout (in the top left corner). The use of GAP elements makes this model work. An initial solution was run, without the presence of GAP elements. The patch and panel vibrated as separate entities, connected only at the rivet locations, and often deformed in opposite directions, passing through one another. This may be what happened to the model described by Henriquez, *et al* [8]. Since their paper did not fully describe the model or the results or even show the mode shapes, but did indicate that the two bolted plates did not appear to be

coupled, this seems likely.

SDRC I-DEAS was used to produce the MSC/NASTRAN bulk data deck and case control deck. Unfortunately, I-DEAS Level V cannot consistently label continuation notation for CELAS2 cards, and does not write the orientation vector properly to the CGAP cards. This required manually verifying the continuation notation for all the CGAP cards, and correcting them when necessary. To fix the CGAP cards, a unit vector was defined in the radial direction of the cylindrical coordinate system to provide orientation for the GAP elements and added to each CGAP card.

IV RESULTS

This chapter will summarize and discuss the resulting solutions of the finite element models in three sections. First, the full panel will be compared to the experimental results of Goodwin and contrasted against prior finite element analysis using NISA. Next, the cutout section models will be compared to the experimental results of Goodwin and contrasted against prior finite element analysis using NISA. Finally, the individual rivet model will be compared to Goodwin's experimental results and contrasted against the perfect bond model and the prior NISA results. Note that a discussion of the effects of the cutout sections on the mode shapes of the panels is not included, since both Goodwin [7] and Cyr [4] provided detailed explanations.

The mode shapes are shown for each model using displacement contours. Although SDRC I-DEAS is capable of producing deformed geometries from the MSC/NASTRAN output files, displacement contours are closely related to the holographic mode shapes provided by experimental analysis and therefore provide a better basis for comparison.

FULL PANEL MODEL

This model, as previously stated, was created to insure that the

modeling procedures used in this analysis represent an accurate approximation of the actual model. The frequency results, which can be seen in Table 6, show that this model is artificially stiff. This, as was

Table 6. Full Panel Results

	f_1	f_2	f_3	f_4	f_5
Full Panel Model (FPM)	558	591	761	825	916
Goodwin Experimental (GE)	514	519	716	727	821
% Difference FPM vs GE	+8.56%	+13.8%	+6.28%	+13.5%	+11.6%
Refined FPM	550	571	755	820	905
% Difference vs GE	+7.00%	+10.0%	+5.45%	+12.8%	+10.2%
NISA (Goodwin)	561	588	797	846	N/A
% Difference vs GE	+9.14%	+13.2%	+11.3%	+16.4%	---

(* all frequencies in hertz)

stated in the theory section, is due to the automatic restraining of the elemental z-axis rotation to insure compatibility. It is evident that refining the model improved the accuracy of the analysis, but doing so increased the cpu time required for the solution by nearly five times (3359.3 vs 15918.3 cpu seconds). The mode shapes for both models are nearly identical, as can be seen in Figures 14 through 23. The mode shapes also match those reported by Goodwin in both his experimental holography work and NISA finite element work. However, both the original and the refined full panel models show closer agreement with the experimental natural frequencies than the NISA results.

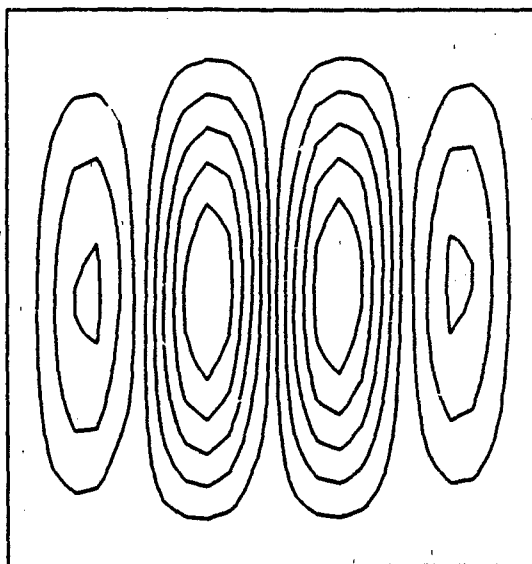


Figure 14. Full Panel Model
Mode 1, $f = 558$ hz

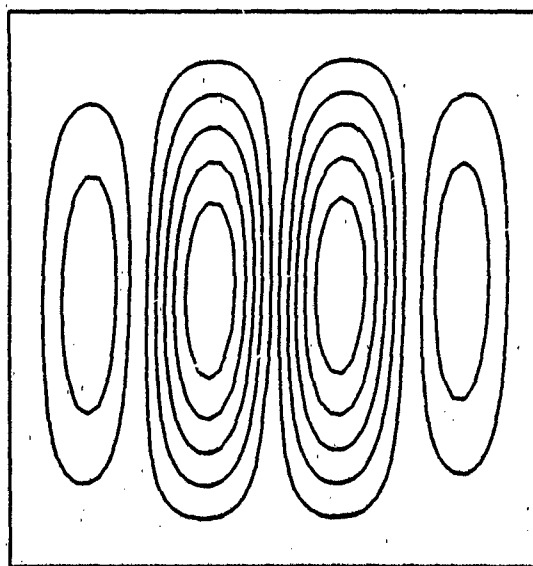
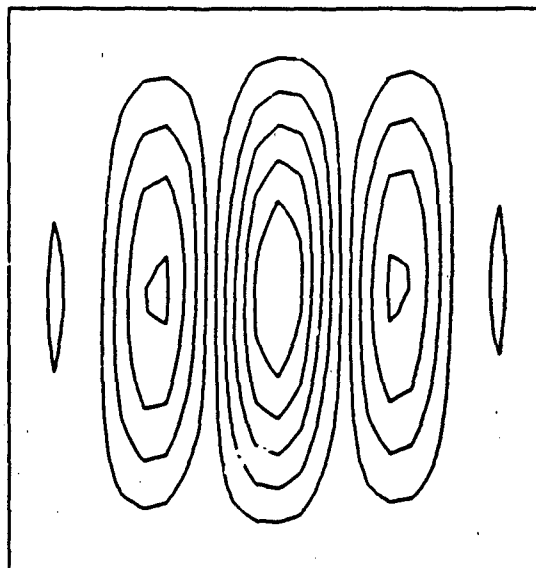
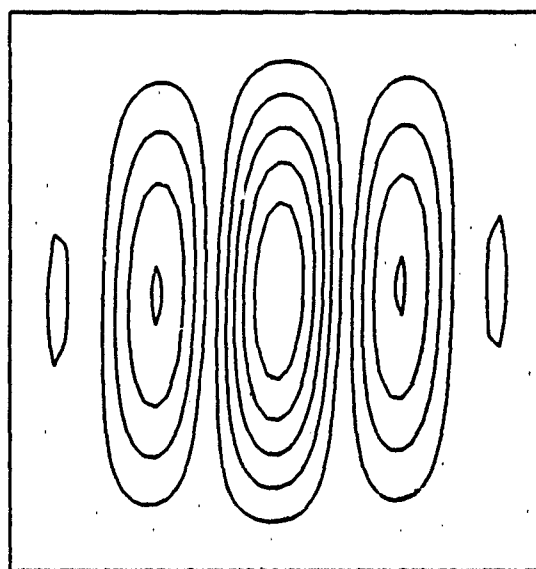


Figure 15. Refined Full Panel Model
Mode 1, $f = 550$ hz



**Figure 16. Full Panel Model
Mode 2, $f = 591$ hz**



**Figure 17. Refined Full Panel Model
Mode 2, $f = 571$ hz**

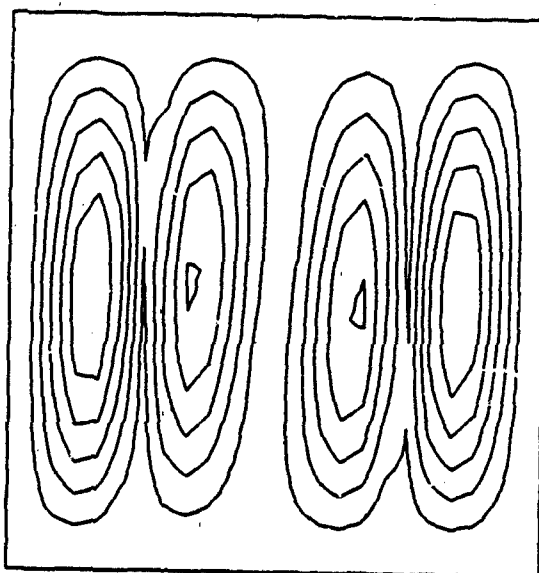


Figure 18. Full Panel Model
Mode 3, $f = 761$ Hz

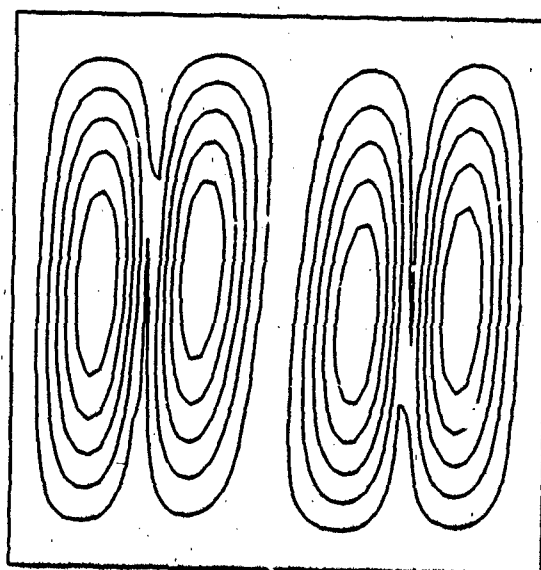


Figure 19. Refined Full Panel Model
Mode 3, $f = 755$ Hz

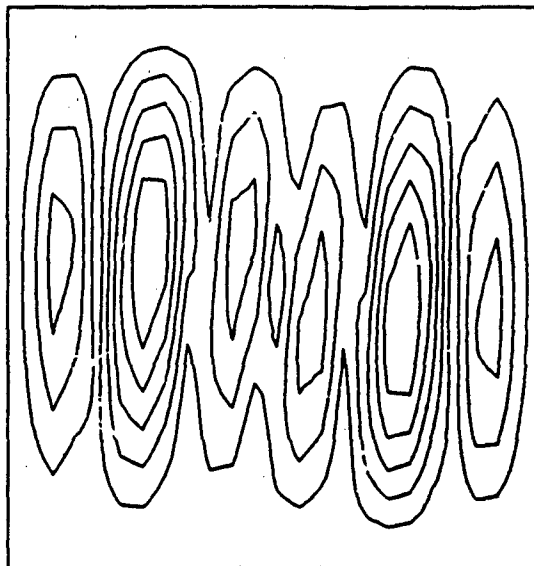


Figure 20. Full Panel Model
Mode 4, $f = 825$ hz

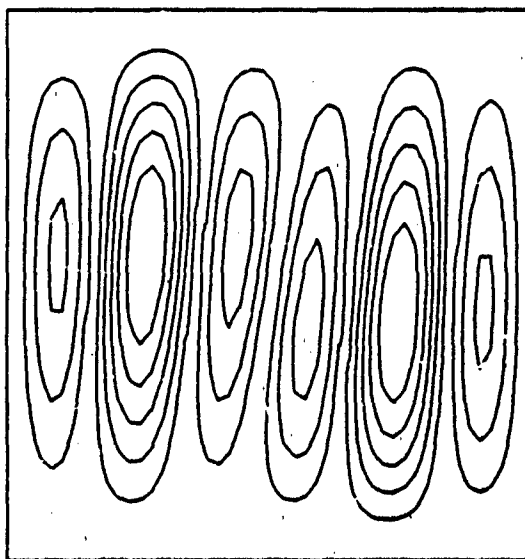
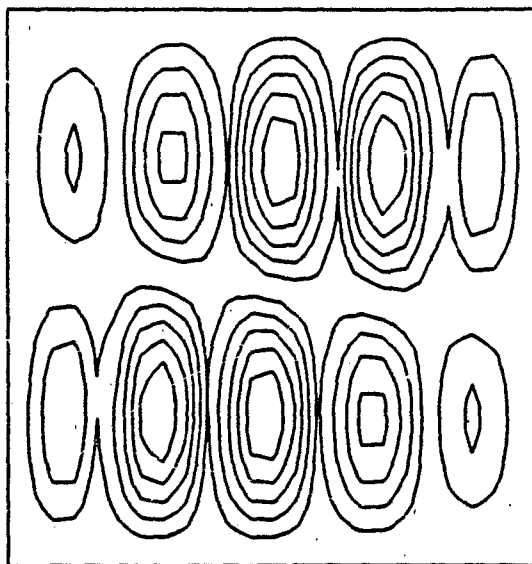
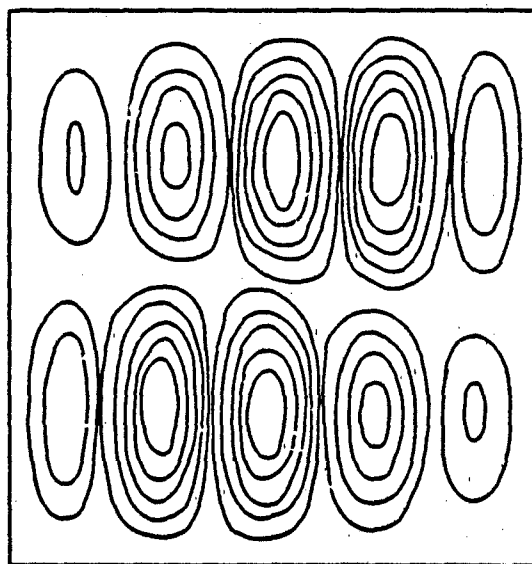


Figure 21. Refined Full Panel Model
Mode 4, $f = 820$ hz



**Figure 22. Full Panel Model
Mode 5, $f = 916$ hz**



**Figure 23. Refined Full Panel Model
Mode 5, $f = 905$ hz**

CUTOUT SECTION MODEL RESULTS

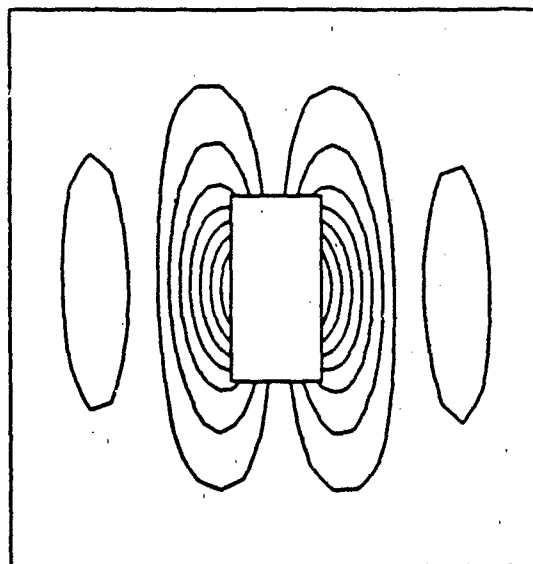
0° CUTOUT SECTION MODEL. The natural frequencies of this model can be found in Table 7. They are, as expected, higher than

Table 7. 0° Cutout Section Model Results

	f_1	f_2	f_3	f_4	f_5
0° Cutout Model	491	560	662	758	812
Goodwin Exper. (GE)	445	507	606	708	749
% Difference	+10.5%	+10.4%	+9.24%	+7.06%	+8.41%
NISA (Goodwin)	499	581	681	789	N/A
% Diff. vs GE	+12.1%	+14.6%	+12.4%	+11.4%	---

(* all frequencies are in hertz)

Goodwin's experimental results and more accurate than Goodwin's NISA results. The mode shapes are shown in Figures 24 through 28. Mode switching is experienced with the second and third mode shapes, relative to Goodwin's experimental work. However, these results agree with Goodwin's NISA work, as well as Cyr's experimental work. As Goodwin noted, mode switching is a phenomenon wherein a symmetric and an adjoining asymmetric mode shape exchange frequencies. It is felt in this instance, though, that Goodwin experienced mode switching in his experimental work, and that the order of mode shapes presented here is the proper one. Also, the second and third mode shapes of this model correspond to the same respective mode shapes of the full panel model.



**Figure 24. 0° Cutout Section Model
Mode 1, $f = 491$ hz**

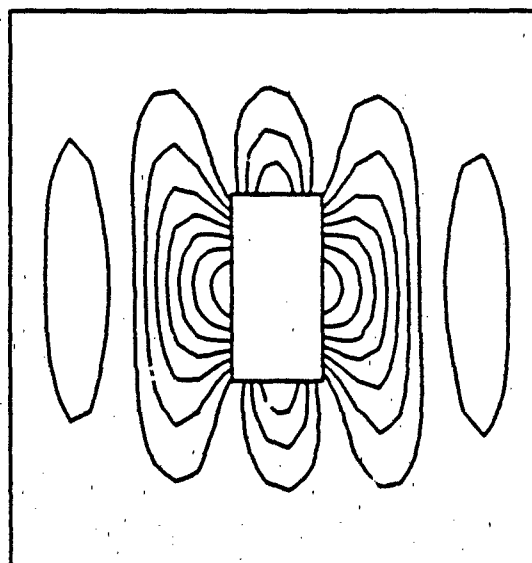


**Figure 25. 0° Cutout Section Model
Mode 2, $f = 560$ hz**

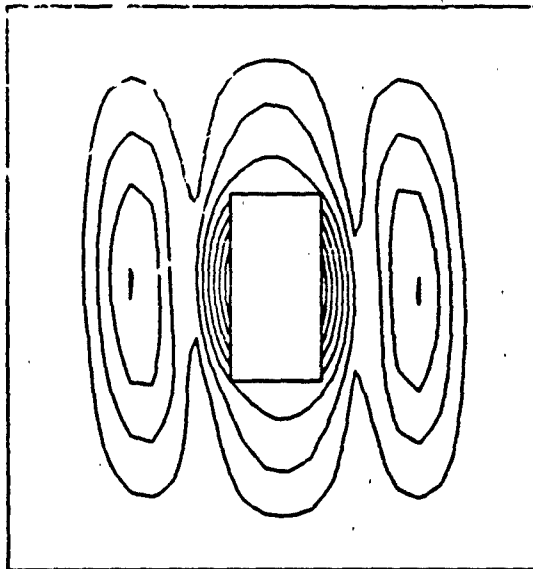


**Figure 26. 0° Cutout Section Model
Mode 3, $f = 662$ hz**

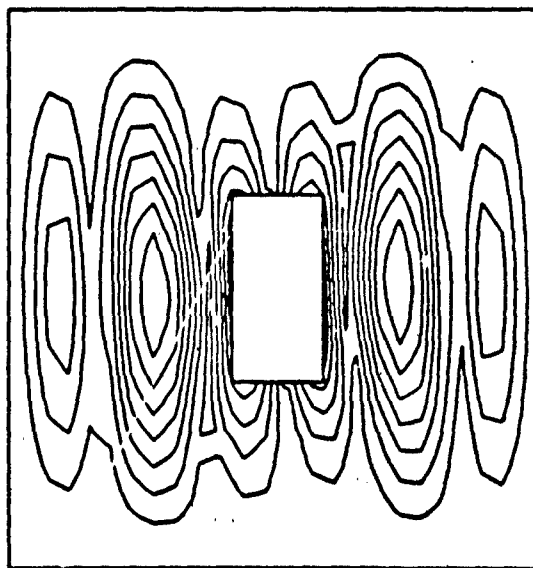


**Figure 27. 0° Cutout Section Model
Mode 4, $f = 758$ hz**

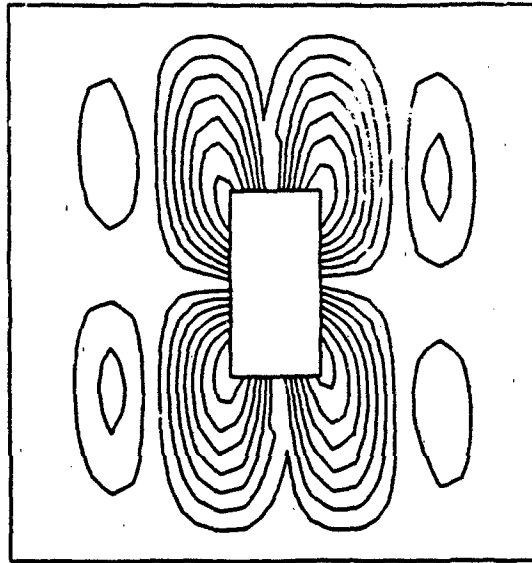


Figure 28. 0° Cutout Section Model
Mode 5, $f = 812$ hz

The effects of the cutout, as are graphed in Figure 29, are least noticeable for the second mode. The general trend agrees with the

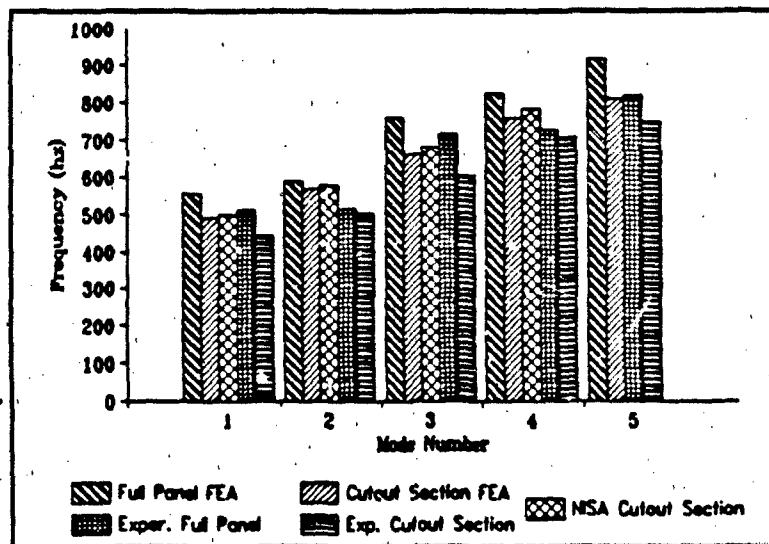


Figure 29. 0° Cutout Effects

experimental work of Goodwin, and the improvement over the NISA results is also obvious.

CUTOUT SECTION MODELS

90° CUTOUT SECTION MODEL. The results of this model do not show perfect agreement with Goodwin's experimental results. The frequency results show that once again the natural frequencies of this model follow the trend of the natural frequencies of the experimental work, only higher. The mode shapes only match Goodwin's results for the first four natural frequencies, although mode switching occurs between the first and second mode shapes. However, this model's first two mode shapes agree with those from Goodwin's NISA work, as well as the first two mode shapes resulting from Cyr's experimental and STAGS C-1 work. Therefore the first four mode shapes were immediately accepted as accurate.

The sixth mode shape of this model, though, matches Goodwin's fifth mode shape while the fifth mode matches nothing. Since Goodwin's fifth mode matches his NISA work, as well as both the experimental and STAGS C-1 FEA work of Cyr, the initial reaction was to regard this new mode shape as a repercussion of this model's use of plate elements to model the curved panel. The mesh was refined and the solution rerun in order to ascertain if increasing the number of degrees of freedom of the model would resolve the situation. The refined mesh frequencies results were

indeed more accurate, as can be seen in Table 8, but the mode shapes did

Table 8. 90° Cutout Section Model

	f_1	f_2	f_3	f_4	f_5
90° Cutout Model	578	582	716	765	779
Goodwin Exp. (GE)	519	546	656	712	733
% Difference	+11.4%	+6.60%	+9.15%	+7.44%	+6.28%
Refined Mesh	570	575	709	744	782
% Diff. vs GE	+9.83%	+5.31%	+8.08%	+5.20%	+3.96%
NISA (Goodwin)	584	585	795	812	N/A
% Diff. vs GE	+12.5%	+7.16%	+21.2%	+14.0%	---

(* all frequencies are in hertz)

not change appreciably, as can be seen in Figures 30 through 41.

As a consequence of the results of the 0° repaired models and the $\pm 45^\circ$ cutout section models (where similar situations occurred), this behavior is now thought to be merely mode switching between this model's fifth and sixth modes. In experimental analysis, mode switching may be a function of the slightest difference in testing conditions, whether it is a slightly different boundary condition or a material imperfection in the test object itself [7:6-11]. For the finite element model, the higher natural frequencies are more sensitive to the boundary conditions [19:232-233]. The artificial restraining of the elemental z-axes for this model could therefore be responsible for the mode switching at higher frequencies.

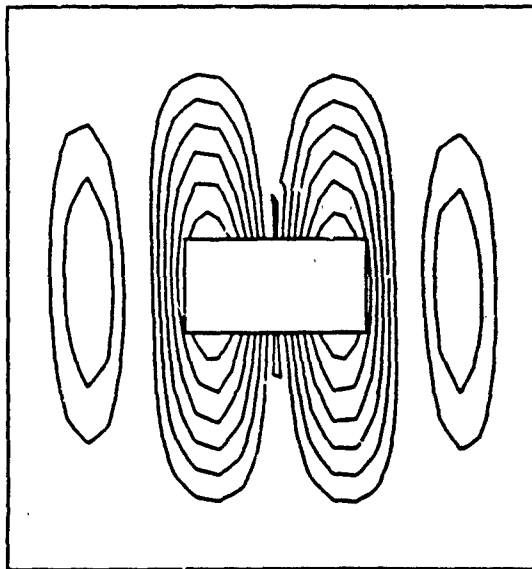


Figure 30. 90° Cutout Section Model
Mode 1, $f = 578$ hz

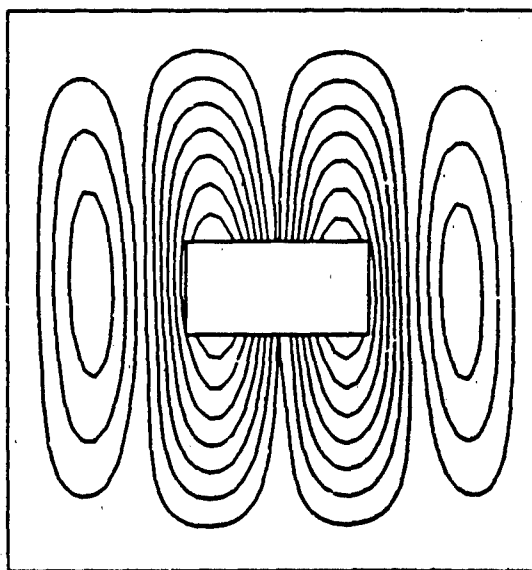
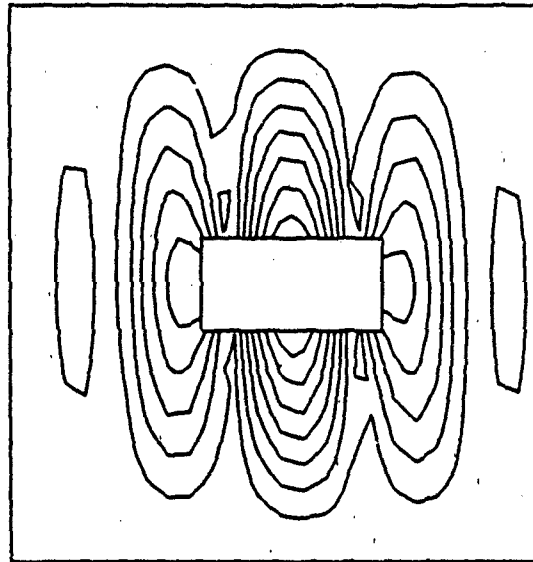
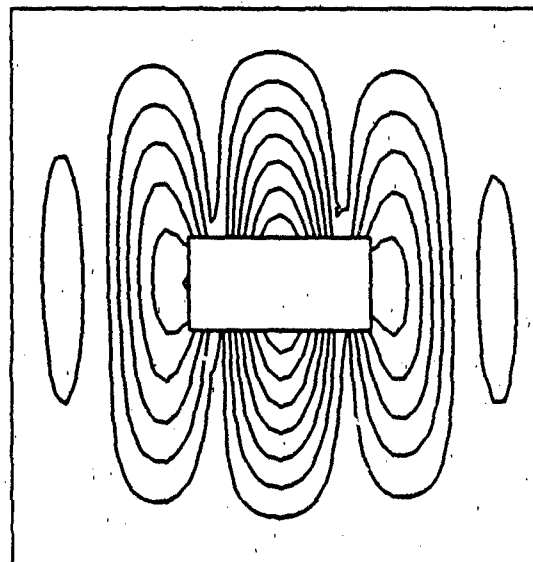


Figure 31. 90° Cutout Section Refined Model
Mode 1, $f = 570$ hz



**Figure 32. 90° Cutout Section Model
Mode 2, $f = 582$ hz**



**Figure 33. 90° Cutout Section Refined Model
Mode 2, $f = 575$ hz**

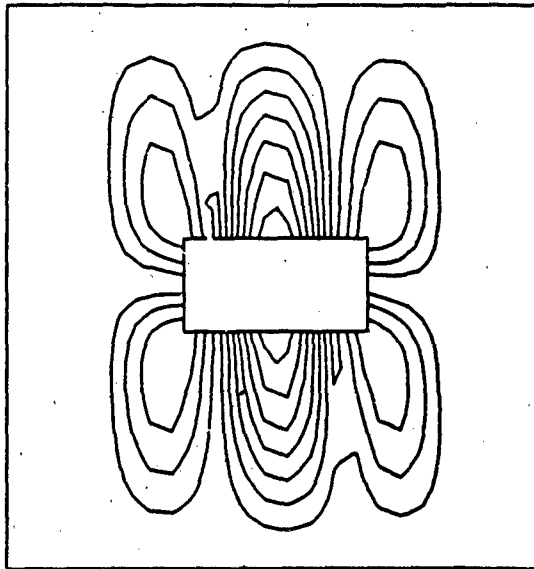


Figure 34. 90° Cutout Section Model
Mode 3, $f = 716$ hz

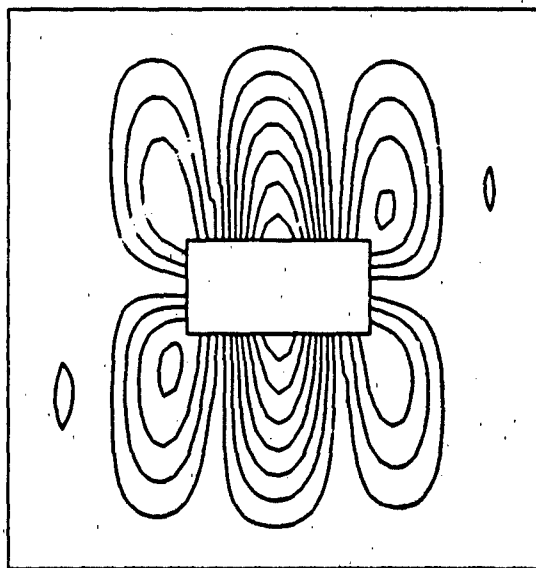


Figure 35. 90° Cutout Section Refined Model
Mode 3, $f = 709$ hz

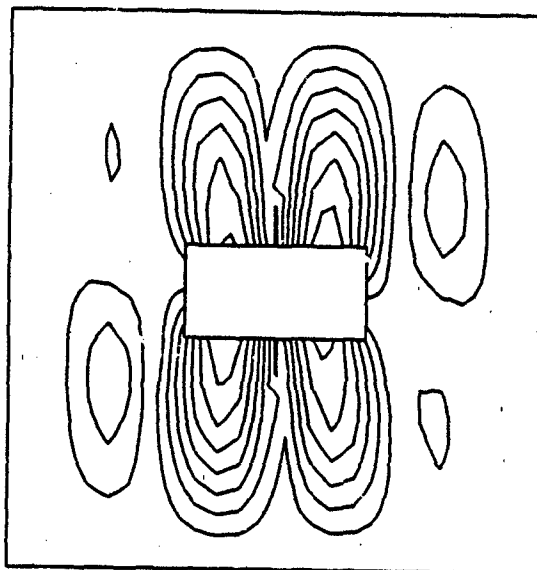


Figure 36. 90° Cutout Section Model
Mode 4, $f = 765$ hz

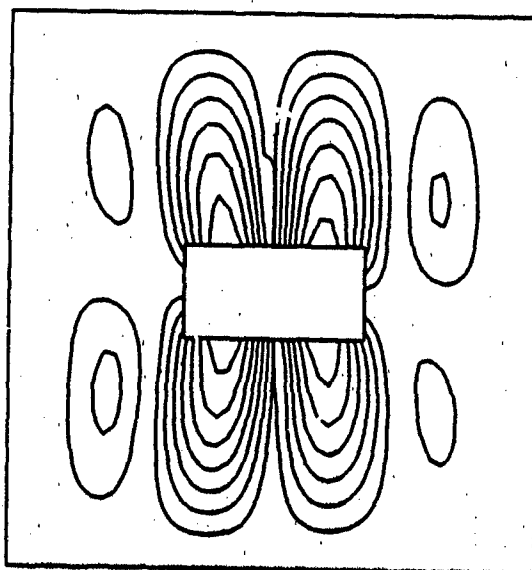


Figure 37. 90° Cutout Section Refined Model
Mode 4, $f = 744$ hz

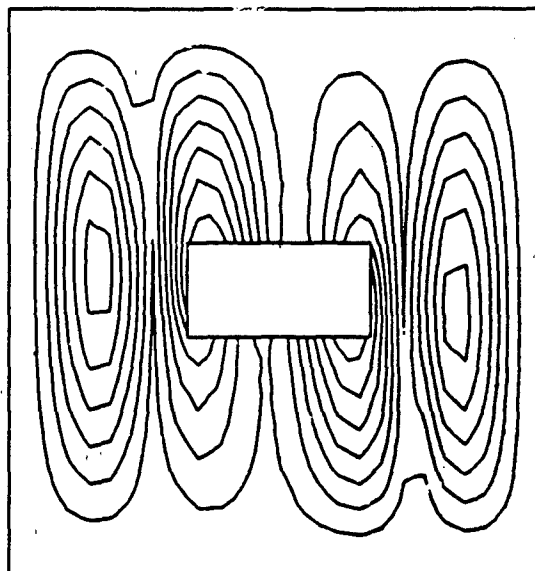


Figure 38. 90° Cutout Section Model
Mode 5, $f = 779$ hz

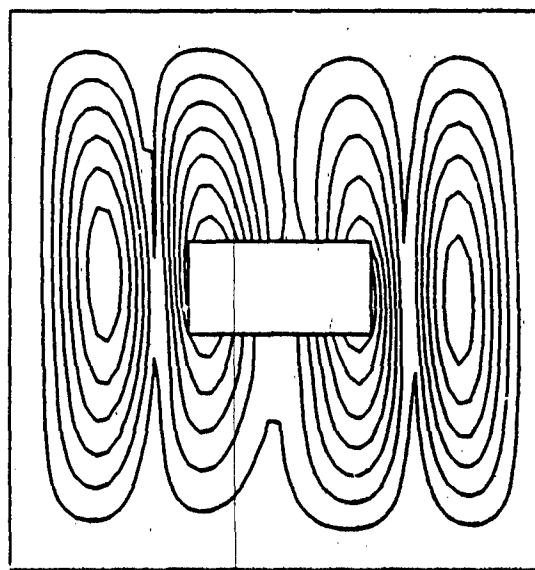


Figure 39. 90° Cutout Section Refined Model
Mode 5, $f = 782$ hz

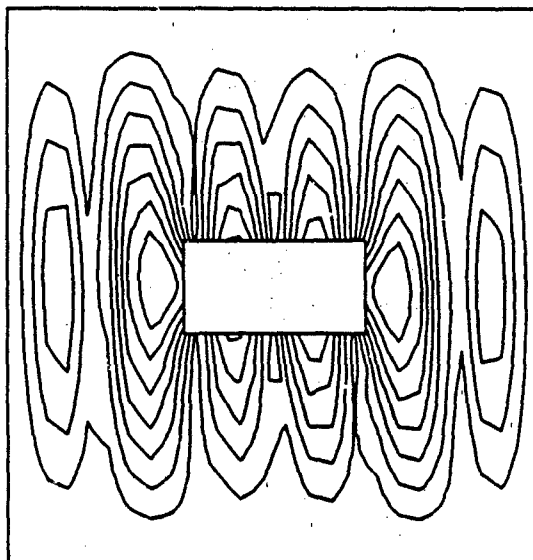


Figure 40. 90° Cutout Section Model
Mode 6, $f = 802$ hz

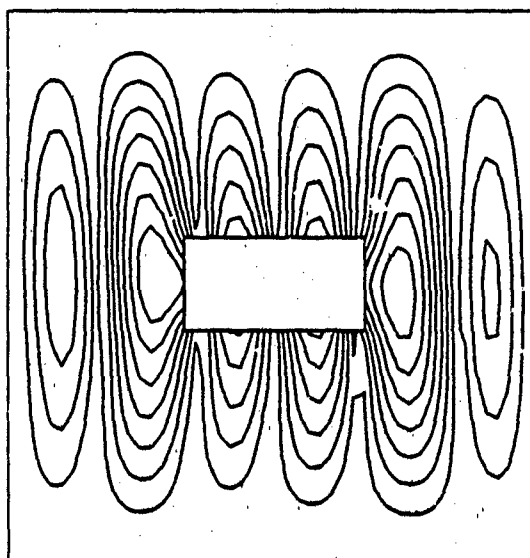


Figure 41. 90° Cutout Section Refined Model
Mode 6, $f = 790$ hz

For this cutout orientation, the first natural frequency is higher than that of the full panel. Goodwin also noted this behavior, although he noted it the first two natural frequencies. As shown graphically in Figure 42,

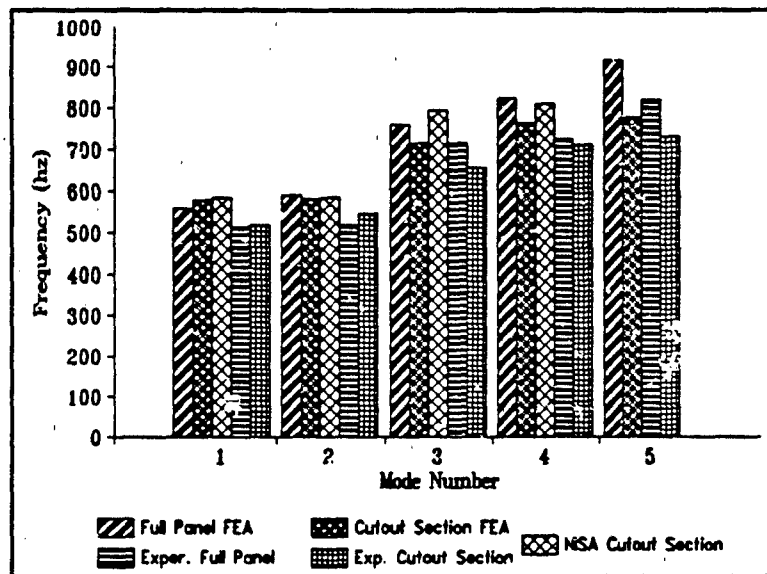


Figure 42. 90° Cutout Effects

this model exhibited nearly the same frequency at the second mode for both the 90° cutout section and the full panel model. Since the natural frequencies are directly proportional to stiffness and inversely proportional to mass, the behavior of this model seems to indicate that more mass was lost than stiffness with the 90° cutout section [6:3032] for the first mode shape. This makes intuitive sense, since the greatest stiffness is provided by the circumferential fibers (the 90° fibers) and the fewest would be damaged by this cutout. Furthermore, the mode shapes become successively more complex, which would emphasize the effects of the lost

stiffness. Because of the mode switching, Goodwin's second mode shape was simpler than his first. This would explain the respectively lower result for the second natural frequency of this model.

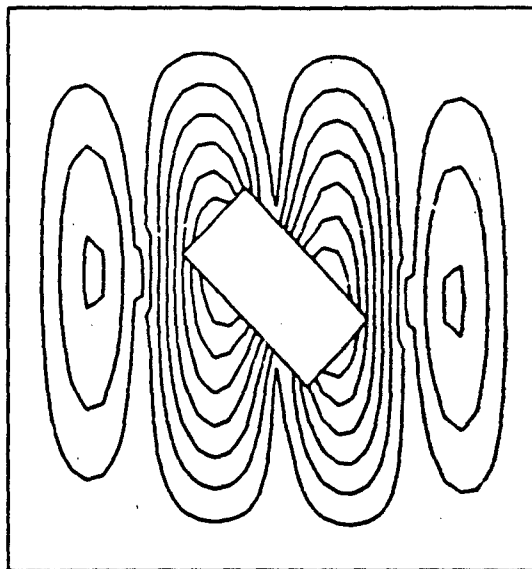
+45° CUTOUT SECTION MODEL. This model displays the same characteristics as the 90° cutout section model, wherein the first four mode shapes match Goodwin's results but the sixth mode shape of this model matches Goodwin's fifth. Similarly, this model's fifth mode matches that found by Cyr in both his experimental and STAGS C-1 FEA work. The natural frequencies of this model, shown in Table 9, are higher than

Table 9. +45° Cutout Section Model Results

	f_1	f_2	f_3	f_4	f_5
+45° Cutout Model	556	592	711	753	823
Goodwin Exper.	500	538	631	685	775
% Difference	+11.2%	+10.0%	+12.7%	+9.93%	+6.19%

(* all frequencies are in hertz)

Goodwin's experimental results, as expected. The mode shapes are shown in Figures 43 through 48. The discrepancy between this model's fifth and sixth modes is considered to be modes switching, especially in light of the results of the -45° cutout section model. The sixth mode of the -45° cutout section model is the transpose of the +45° cutout section model's fifth mode shape and matches the fifth mode shape predicted by Cyr's STAGS C-1 work. This will be more fully explained in the next section.



**Figure 43. +45° Cutout Section Model
Mode 1, $f = 556$ hz**

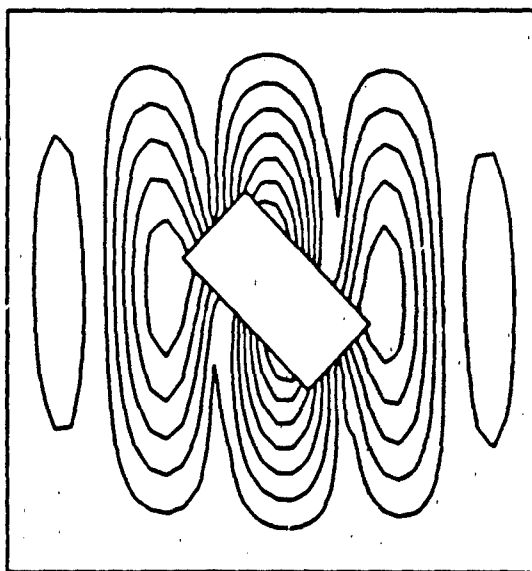


**Figure 44. +45° Cutout Section Model
Mode 2, $f = 592$ hz**

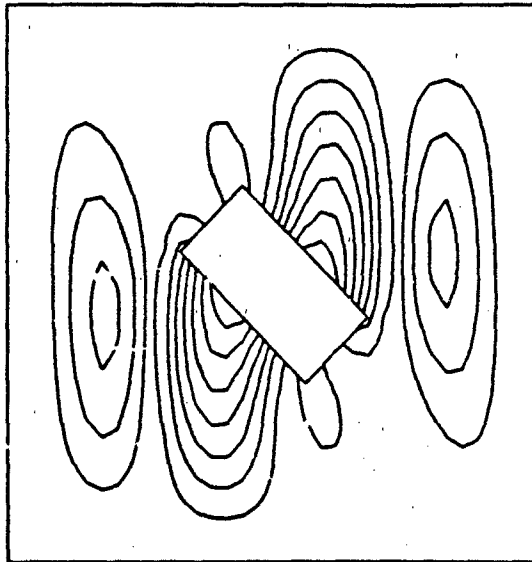


**Figure 45. +45° Cutout Section Model
Mode 3, $f = 711$ Hz**

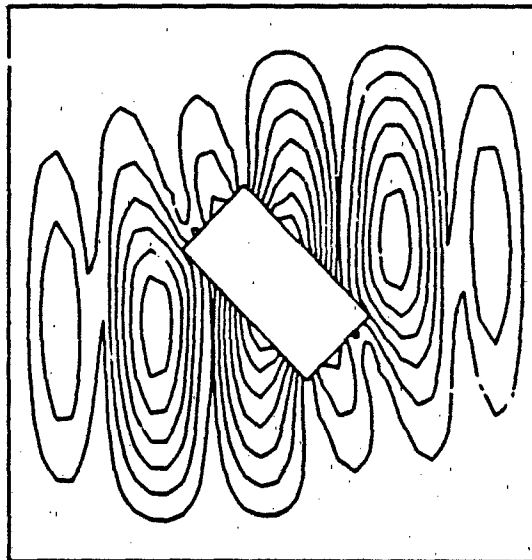


**Figure 46. +45° Cutout Section Model
Mode 4, $f = 753$ Hz**

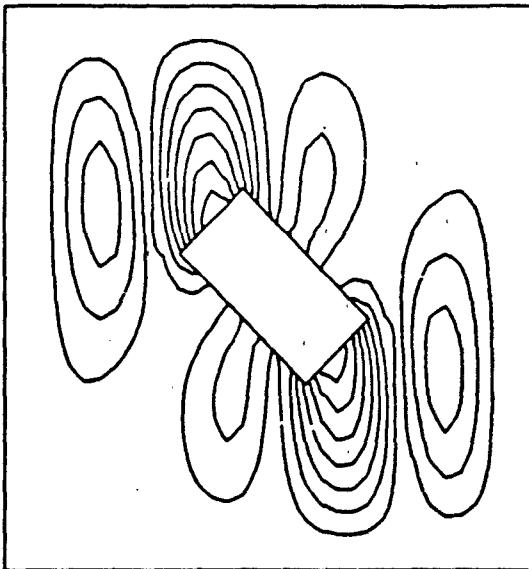


**Figure 47. +45° Cutout Section Model
Mode 5, $f = 823$ Hz**

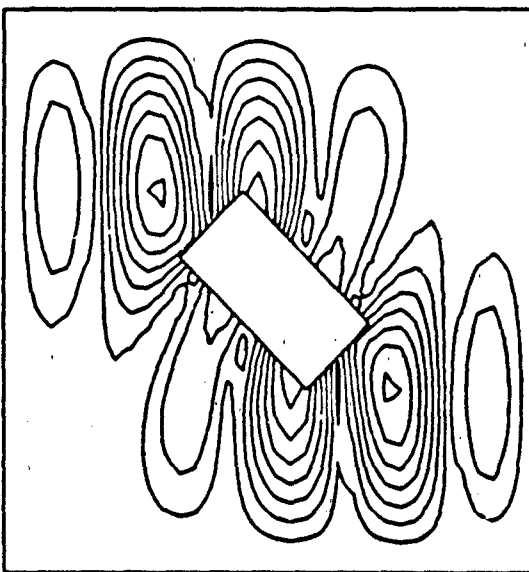


**Figure 48. +45° Cutout Section Model
Mode 6, $f = 850$ Hz**

The +45° cutout section caused a loss in stiffness for all the modes, as compared to full panel model. This agrees with the trend of Goodwin's work, as is shown in Figure 49. Both show a decrease in the first natural frequency and an increase in the second, as compared to the full panel results. Note that the NISA code was extremely limited and unable to model this configuration.

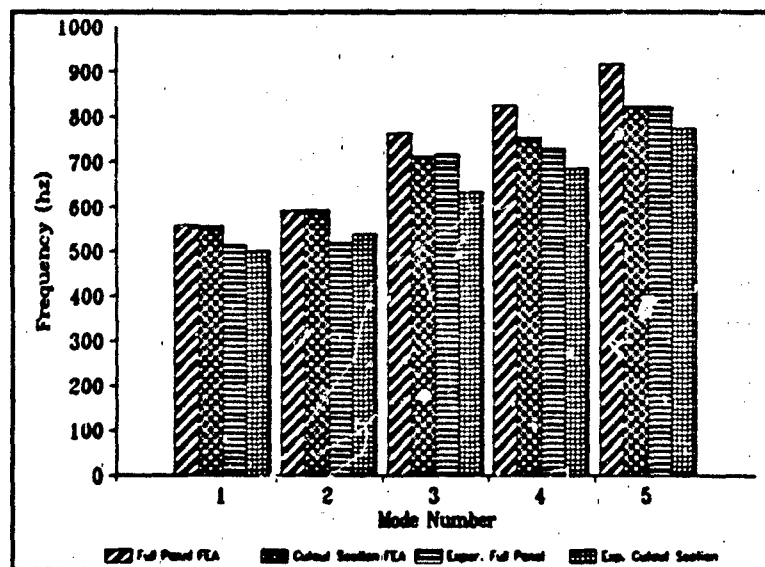


Figure 49. +45° Cutout Effects

-45° CUTOUT SECTION MODEL. This is one of the most interesting models. Its natural frequencies more closely match Goodwin's than any other cutout (see Table 10), and it sheds light on the higher-frequency mode switching phenomenon.

Table 10. -45° Cutout Section Model Results

	f_1	f_2	f_3	f_4	f_5
-45° Cutout Model	550	584	698	749	818
Goodwin Exper.	528	538	648	666	823
% Difference	+4.17%	+8.55%	+7.72%	+12.5%	-0.607%

(* all frequencies are in hertz)

Its first five mode shapes match those found by Goodwin's experimental work as well as those found by the STAGS C-1 work of Cyr. Its first four mode shapes match the first four of Cyr's experimental work, and this model's sixth mode shape matches Cyr's fifth experimental mode shape. It appears that Cyr experienced mode switching with his fifth mode but never noticed it, since he never investigated the sixth mode. Rajamani and Prabhakaran noted a relationship between mode switching at higher frequencies and cutout orientation, and perhaps this model is more sensitive to such behavior due to its unique boundary condition [16:576]. The order of mode shapes presented here in Figures 50 through 55 is thought to be the proper one.

It is also interesting to note that the mode shapes for the -45° cutout section model are the transposes of those for the +45° model, except that the fifth and sixth mode shape are switched, as was previously noted.

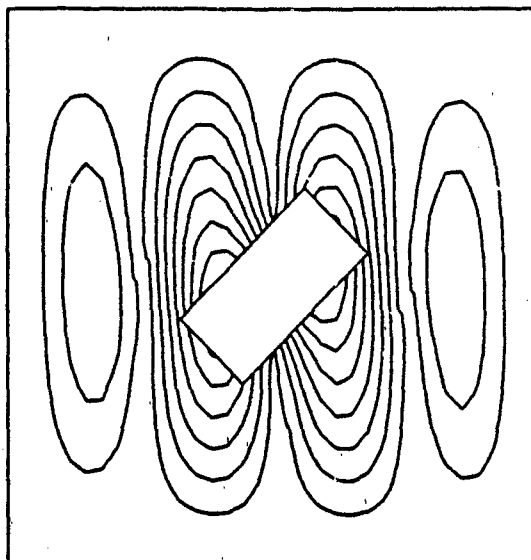


**Figure 50. -45° Cutout Section Model
Mode 1, $f = 550$ Hz**

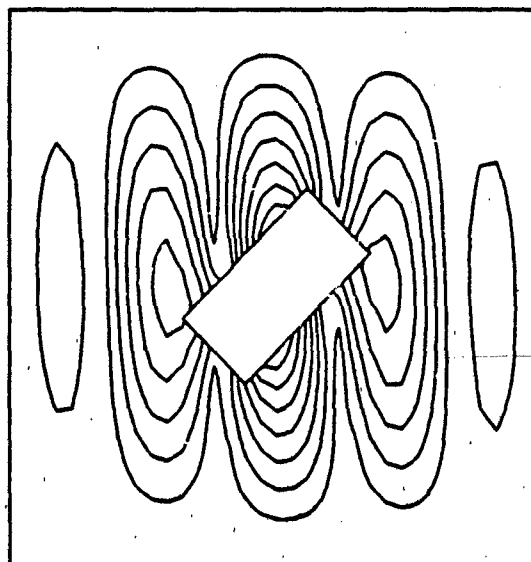


**Figure 51. -45° Cutout Section Model
Mode 2, $f = 584$ Hz**

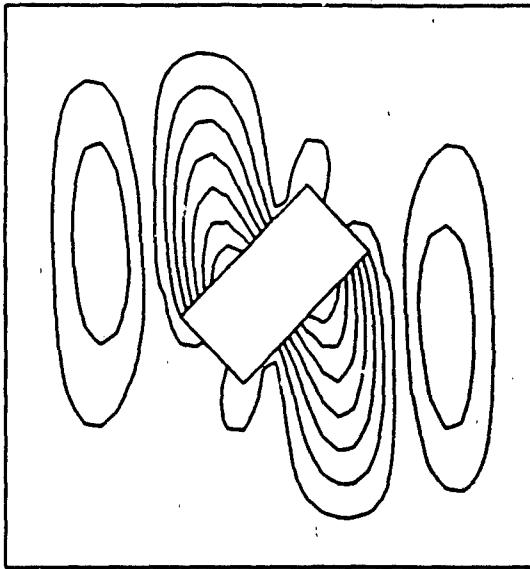


**Figure 52. -45° Cutout Section Model
Mode 3, $f = 698$ hz**

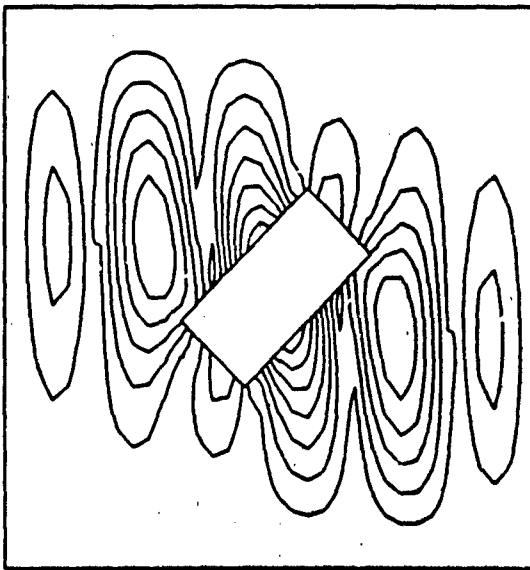


**Figure 53. -45° Cutout Section Model
Mode 4, $f = 749$ hz**

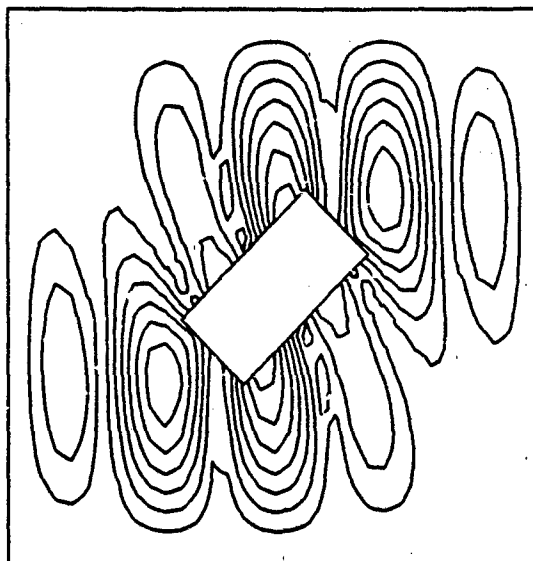


**Figure 54. -45° Cutout Section Model
Mode 5, $f = 818$ hz**

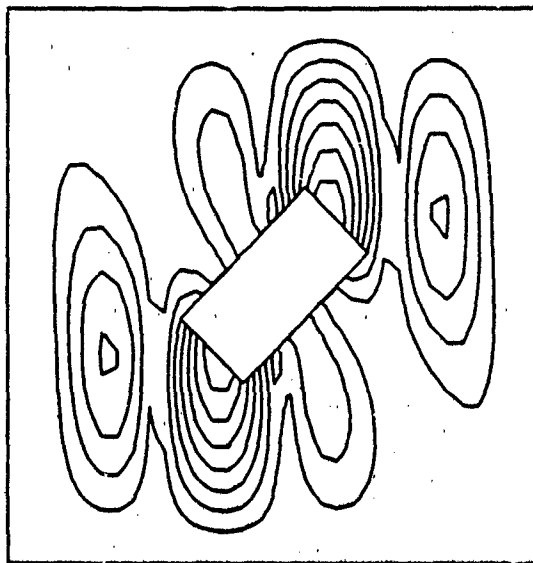


**Figure 55. -45° Cutout Section Model
Mode 6, $f = 819$ hz**

Unlike Goodwin's results, this model shows a noticeable decrease in natural frequency for the first two mode shapes as compared to the full panel model as in shown in Figure 56. However, the experimental

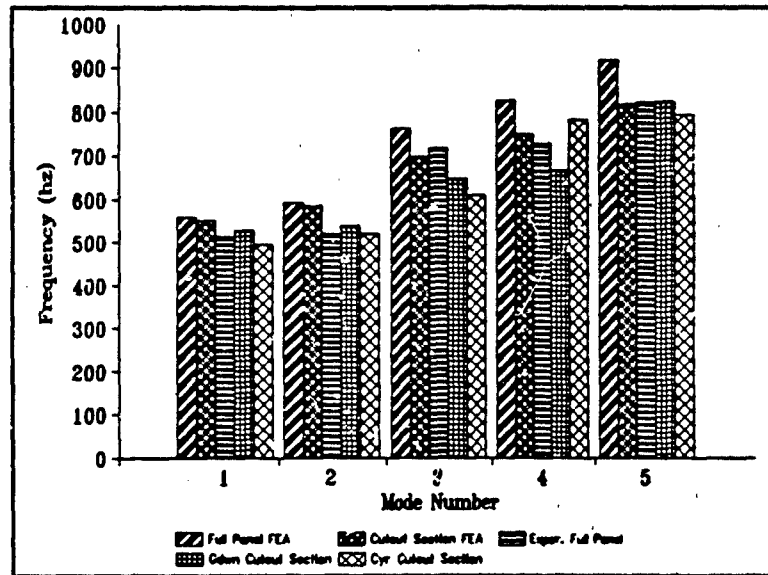


Figure 56. -45° Cutout Effects

results of Cyr also showed a noticeable decrease which he attributed to a poorly clamped test condition. It would make sense for the natural frequencies to increase as they did for the +45° model, since the laminate is a quasi-isotropic layup. However, the results for the -45° orientation are close enough to those of for the +45° orientation for the first two modes (less than 1.5% in each case) that this difference can be attributed to slight differences when defining the geometries for the models and numeric error in the solution process.

REPAIRED PANEL MODELS

0° REPAIRED PANEL MODEL. This repair orientation proved the presence of mode switching between the fifth and sixth mode shapes, although that was not immediately obvious. Initially, the perfect bond model and individual rivet model were solved and compared. An extra mode shape occurred in the individual rivet model solution between Goodwin's fourth and fifth mode shapes. The mesh was refined so that the elements were approximately $\frac{1}{4}$ " square (see Figure 57) and the model

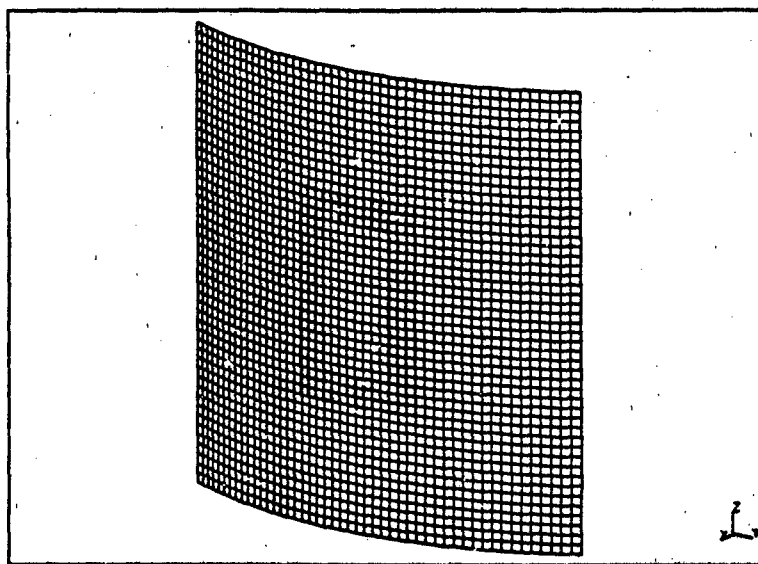


Figure 57. Refined 0° Patch Model

rerun. The natural frequencies were more accurate (see Table 11), but the additional mode shape remained. The first six mode shapes for both models were then examined in close detail.

Table 11. 0° Repair Model Results

	f_1	f_2	f_3	f_4	f_5
Rivet Model	460	531	702	780	830
Goodwin Exp. (GE)	439	555	663	745	795
% Difference	+4.78%	-4.32%	+5.88%	+4.70%	+4.40%
Refined Rivet Model	447	522	689	757	815
% Diff. vs GE	+1.82%	-5.95%	+3.92%	+1.61%	+2.52%
Perfect Bond Model	537	600	779	928	954
% Diff. vs GE	+22%	+8.2%	+17%	+24%	+20%
NISA	490	549	730	884	N/A
% Diff. vs GE	+11.6%	-1.08%	+10.1%	+18.7	---

(* all frequencies in hertz)

The perfectly bonded repair model resulted in mode shapes that matched Goodwin's experimental and FEA results, although the associated natural frequencies were very high. The individual rivet model, however, agreed with Goodwin for the first four mode shapes, but showed Goodwin's fifth mode shape at the sixth natural frequency. Also, the fifth mode shape of the individual rivet model matched the sixth mode shape of the perfectly bonded model. This verified that the extra mode shape was the result of mode switching. These individual rivet model mode shapes are compared against the perfect bond model mode shapes in Figures 57 through 69. The refined rivet model mode shapes are shown in Figures 70 through 75.

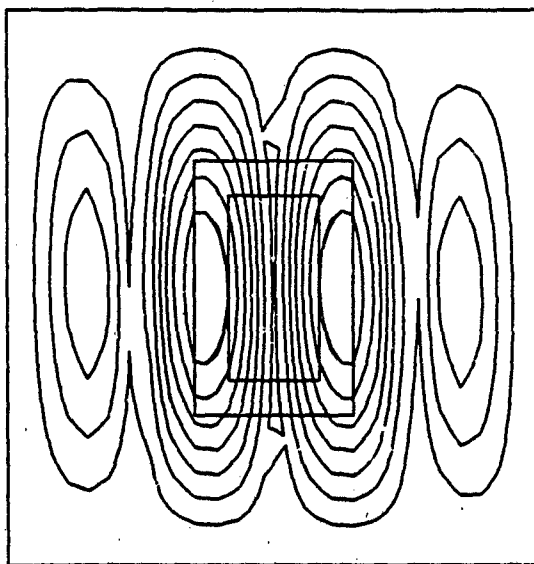


Figure 58. 0° Repair Individual Rivet Model
 Mode 1, $f = 460$ hz

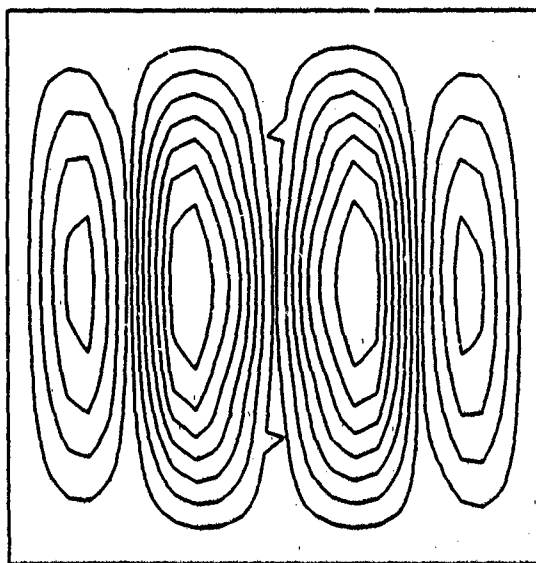


Figure 59. 0° Repair Perfect Bond Model
 Mode 1, $f = 537$ hz

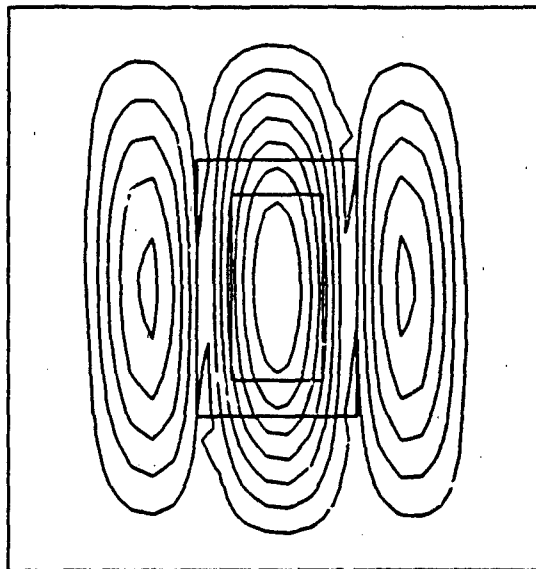


Figure 60. 0° Repair Individual Rivet Model
Mode 2, $f = 531$ hz

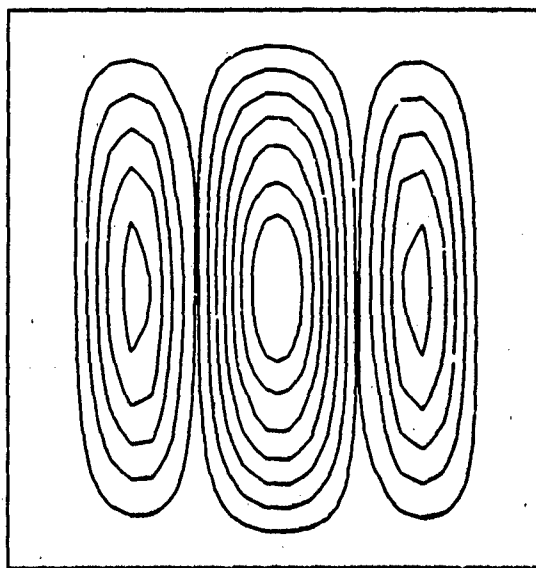


Figure 61. 0° Repair Perfect Bond Model
Mode 2, $f = 600$ hz

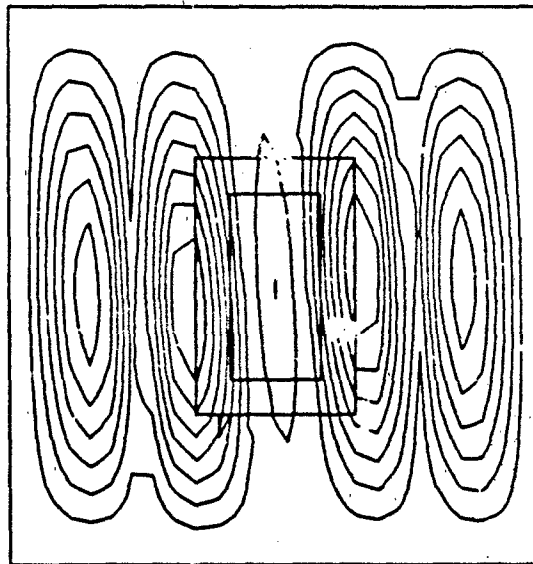


Figure 62. 0° Repair Individual Rivet Model
Mode 3, $f = 702$ hz

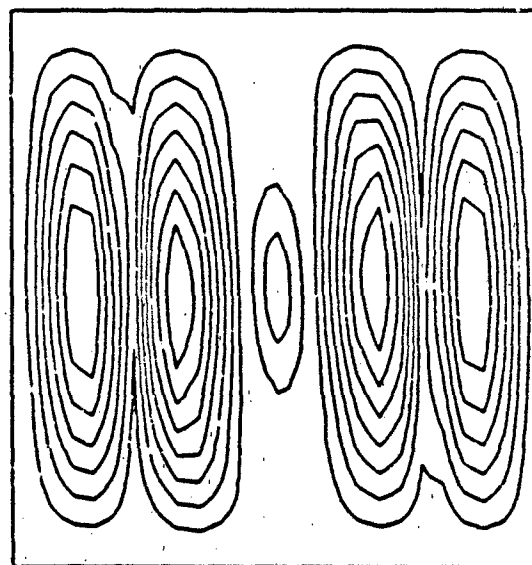


Figure 63. 0° Repair Perfect Bond Model
Mode 3, $f = 779$ hz

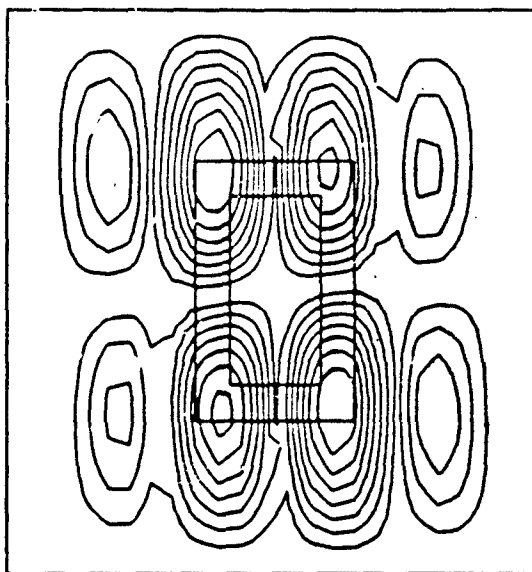


Figure 64. 0° Repair Individual Rivet Model
Mode 4, $f = 780$ hz

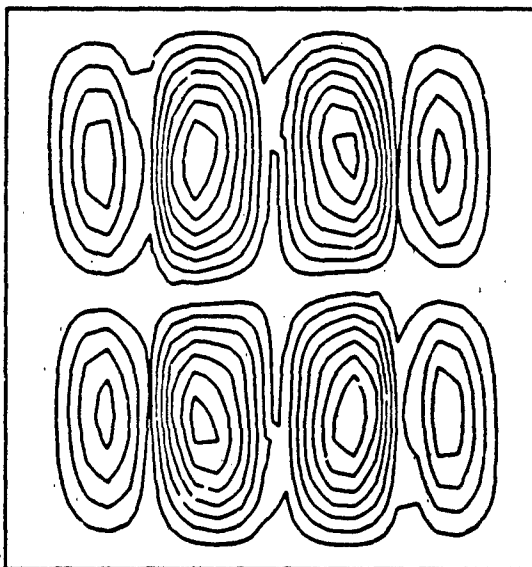
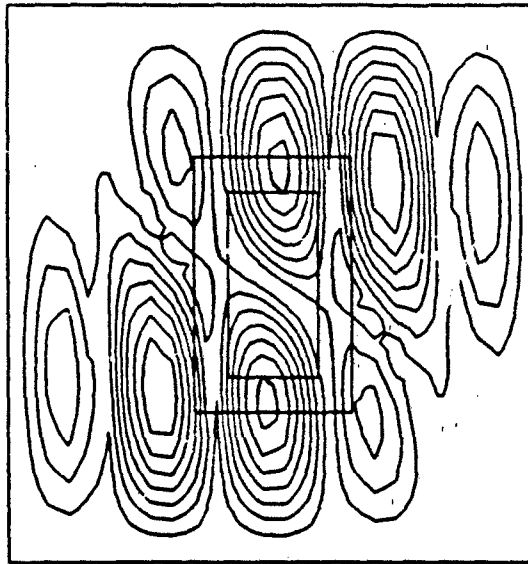
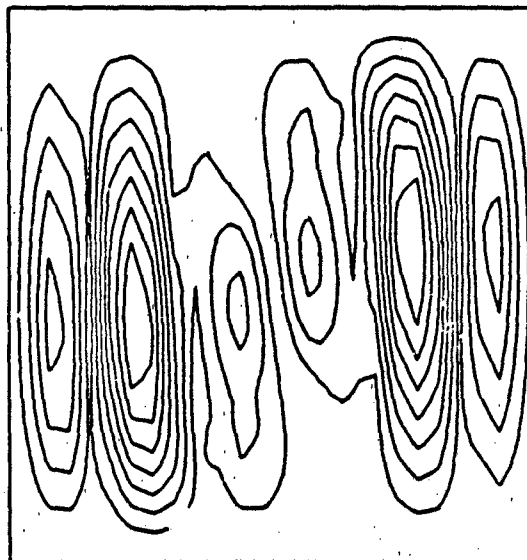


Figure 65. 0° Repair Perfect Bond Model
Mode 4, $f = 928$ hz



**Figure 66. 0° Repair Individual Rivet Model
Mode 5, $f = 830$ hz**



**Figure 67. 0° Repair Perfect Bond Model
Mode 5, $f = 954$ hz**

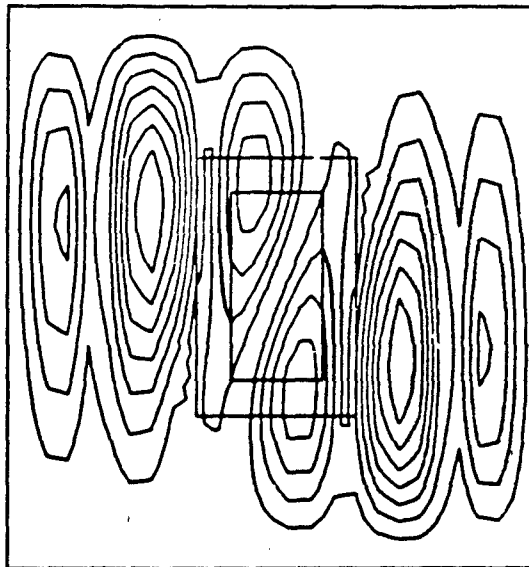


Figure 68. 0° Repair Individual Rivet Model
Mode 6, $f = 853$ hz

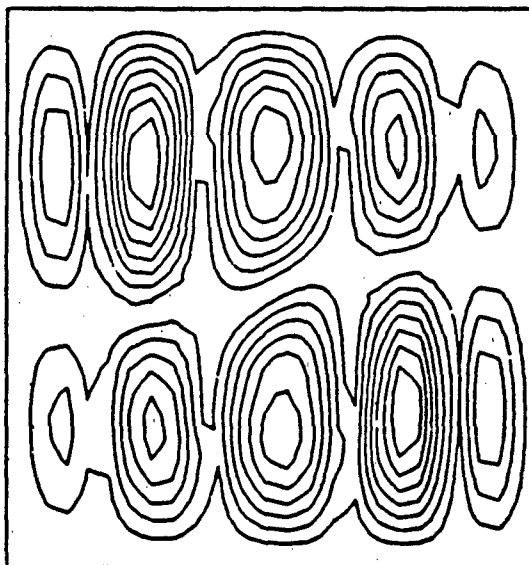
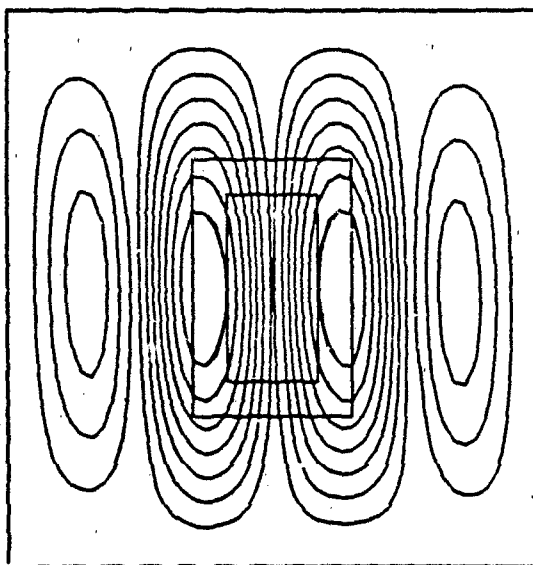
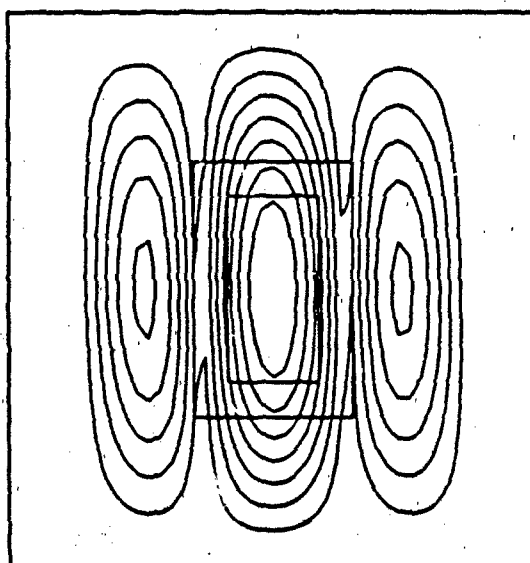


Figure 69. 0° Repair Perfect Bond Model
Mode 6, $f = 992$ hz



**Figure 70. 0° Repair Refined Rivet Model
Mode 1, $f = 447$ hz**



**Figure 71. 0° Repair Refined Rivet Model
Mode 2, $f = 522$ hz**

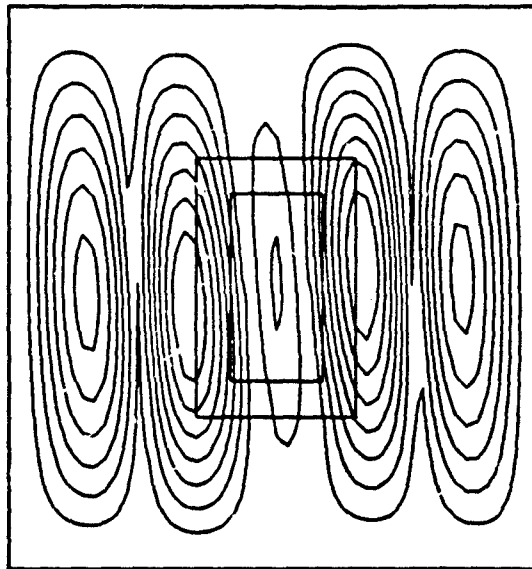


**Figure 72. 0° Repair Refined Rivet Model
Mode 3, $f = 689$ hz**

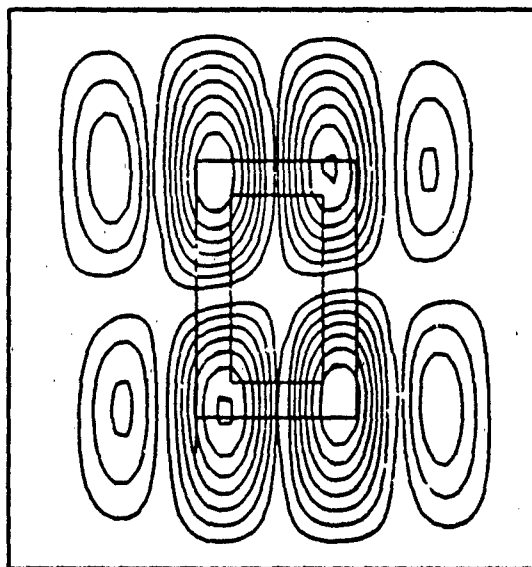


**Figure 73. 0° Repair Refined Rivet Model
Mode 4, $f = 757$ hz**

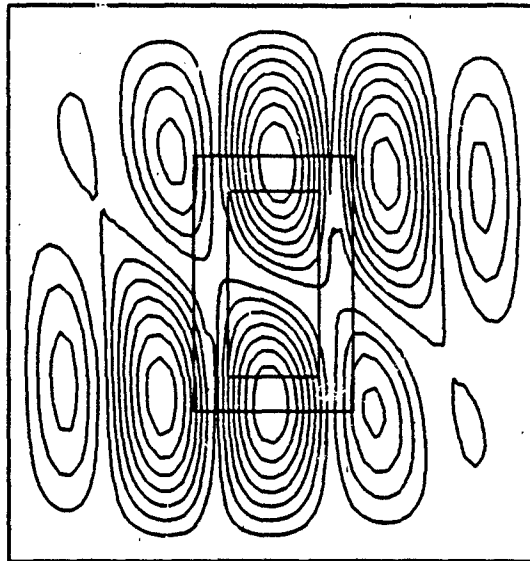


**Figure 74. 0° Repair Refined Rivet Model
Mode 5, $f = 815$ hz**

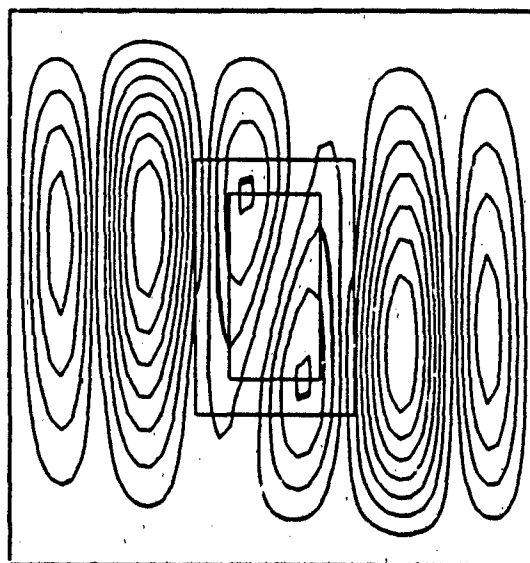


**Figure 75. 0° Repair Refined Rivet Model
Mode 6, $f = 849$ hz**

The graph in Figure 76 show that individually modeling the rivets more closely approximates the actual behavior of the panel while the assuming a perfect bond continues the trend set by the NISA results by being consistently and increasingly too stiff. This makes sense, since the patch is only "bonded" to the panel at the rivets.

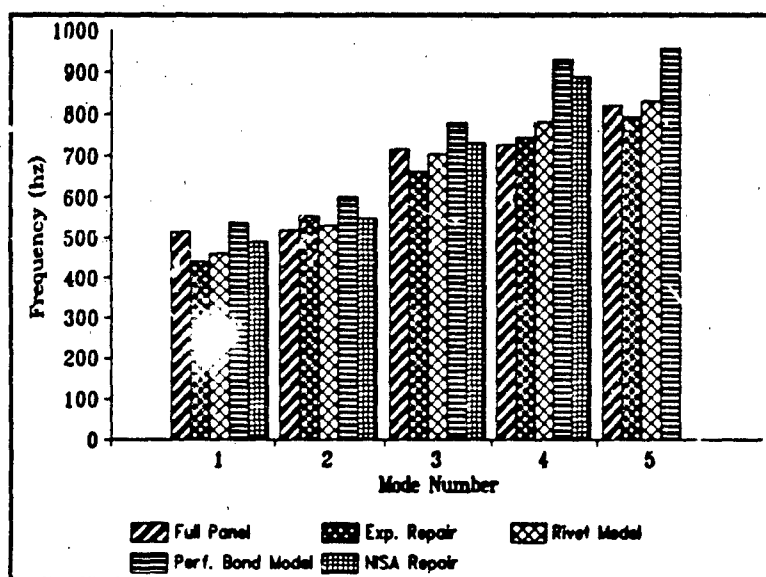


Figure 76. 0° Repair Effects.

90° REPAIRED PANEL MODELS. The natural frequencies of the individual rivet model are a substantial improvement over the perfect bond model and a good approximation of the actual conditions, as shown in Table 12. Both the individual rivet model and the perfect bond model show mode switching between modes four and five with respect to Goodwin's experimental work. They agree with the mode shapes as predicted by

Table 12. 90° Repair Model Results

	f_1	f_2	f_3	f_4	f_5
Rivet Model	475	506	710	759	828
Goodwin Exp. (GE)	509	523	706	758	796
% Difference	-6.67%	-3.25%	+0.566%	+0.132%	+4.02%
Perf. Bond Model	592	616	817	955	978
% Diff. vs GE	+16%	+18%	+16%	+26%	+23%
NISA	500	535	749	800	N/A
% Diff. vs GE	-1.77%	+2.29%	+6.09%	+5.54%	---

(* all frequencies are in hertz)

Goodwin's NISA work, and they are consistent with the full panel mode shapes. These circumstances show that Goodwin experienced mode switching between his fourth and fifth mode shapes in his experimental work. The mode shapes shown here are therefore felt to be ordered in the proper arrangement. The mode shapes are presented in Figures 77 through 86.

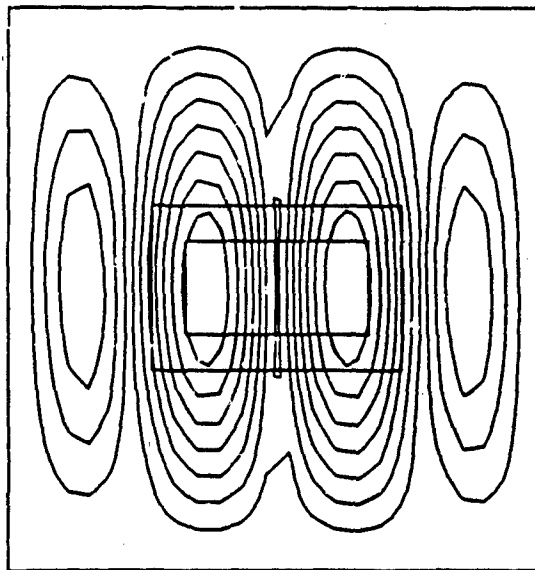


Figure 77. 90° Repair Individual Rivet Model
Mode 1, $f = 475$ hz

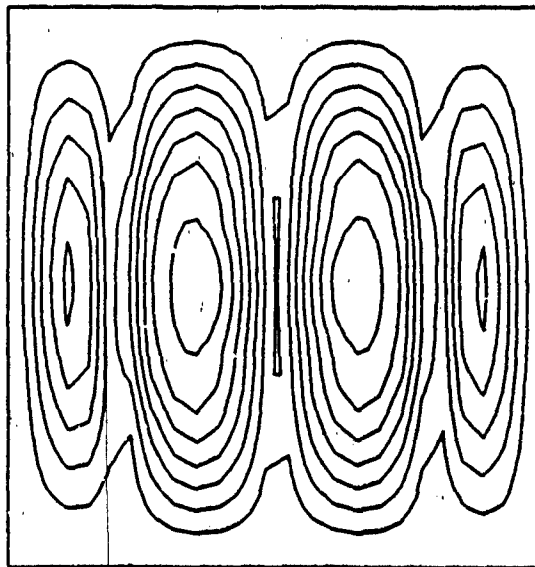


Figure 78. 90° Repair Perfect Bond Model
Mode 1, $f = 592$ hz

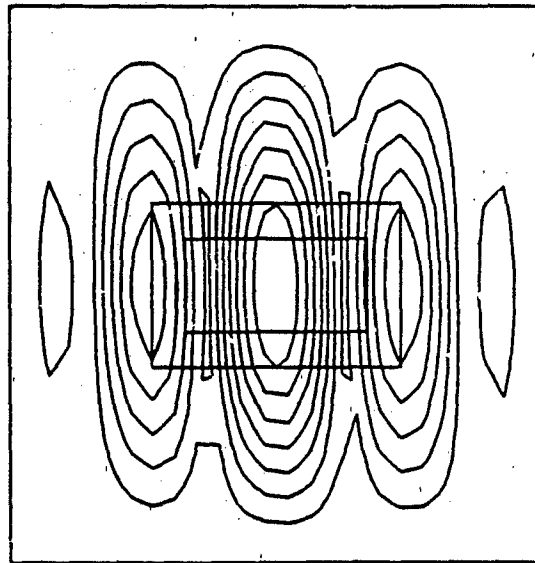


Figure 79. 90° Repair Individual Rivet Model
Mode 2, $f = 506$ hz

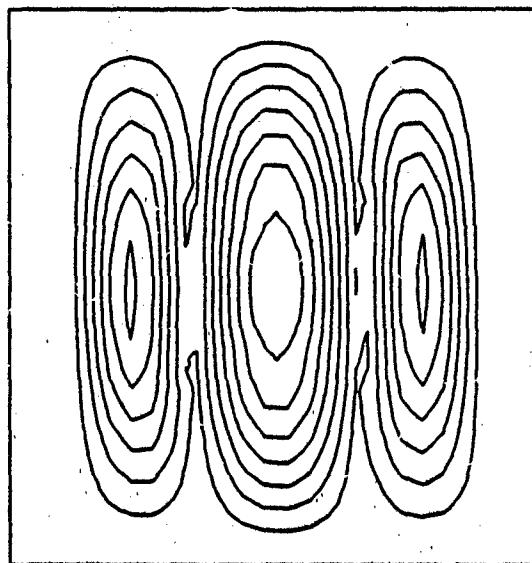
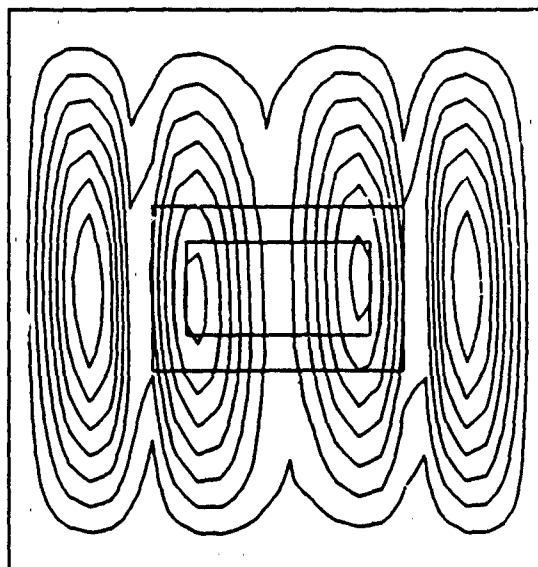
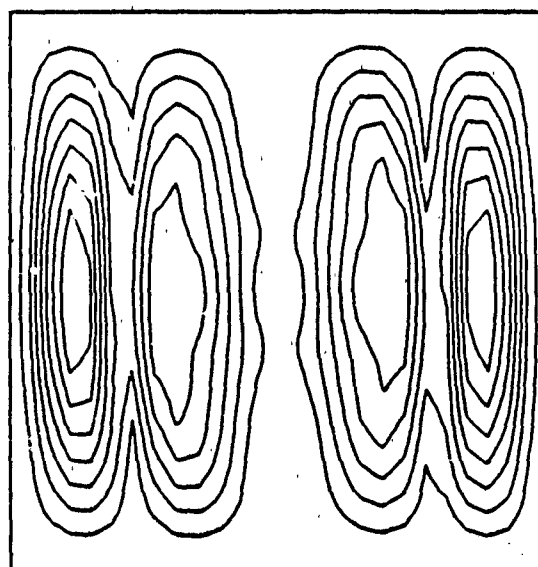


Figure 80. 90° Repair Perfect Bond Model
Mode 2, $f = 506$ hz



**Figure 81. 90° Repair Individual Rivet Model
Mode 3, $f = 710$ hz**



**Figure 82. 90° Repair Perfect Bond Model
Mode 3, $f = 817$ hz**

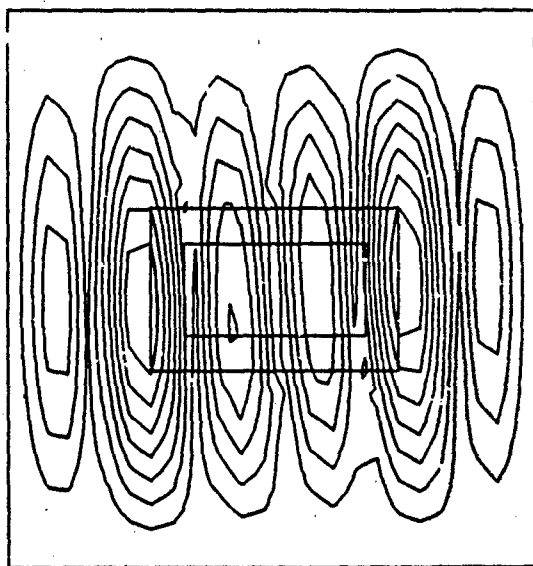


Figure 83. 90° Repair Individual Rivet Model
Mode 4, $f = 759$ hz

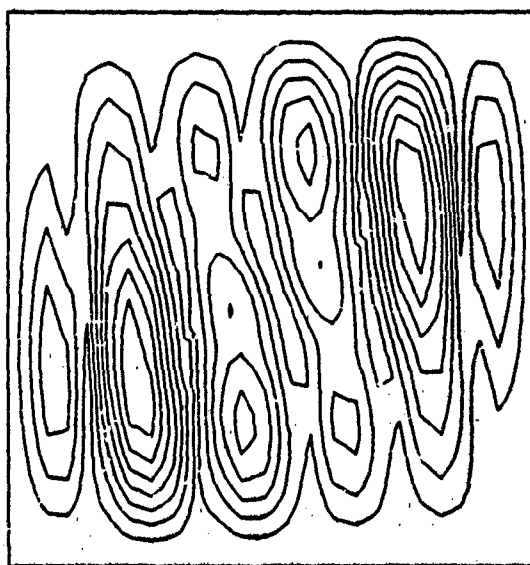


Figure 84. 90° Repair Perfect Bond Model
Mode 4, $f = 955$ hz

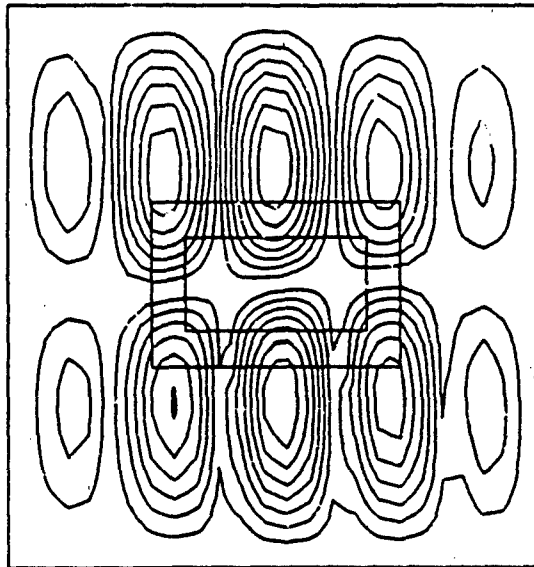


Figure 85. 90° Repair Individual Rivet Model
Mode 5, $f = 828$ hz

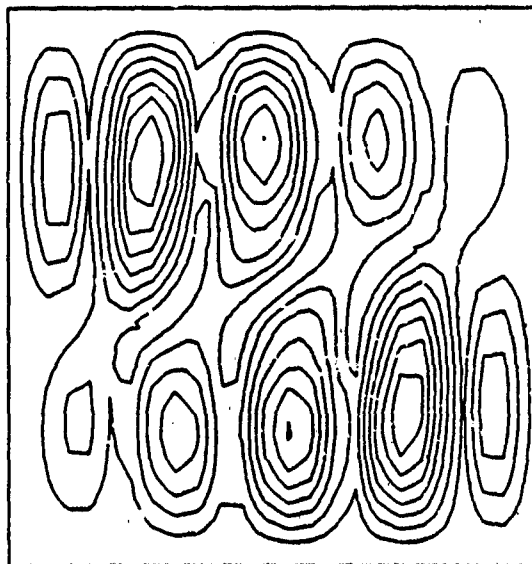


Figure 86. 90° Repair Perfect Bond Model
Mode 5, $f = 978$ hz

Figure 87 allows a graphic comparison of the frequency results. The most striking feature is that the first two natural frequencies of the individual rivet model were lower than the first two natural frequencies reported by Goodwin for his experimental work. This is unusual because the models using QUAD4 elements have been unnaturally stiff before this.

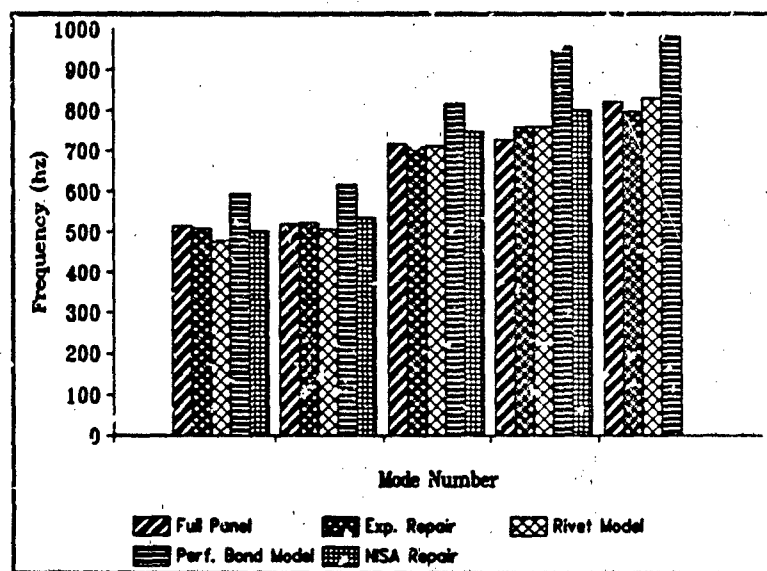


Figure 87. 90° Repair Effects

Since this 90° orientation causes the patch to cross more node lines than the 0° orientation, the presence of the CONM2 elements at the rivet locations could be responsible for this drop in the first two natural frequencies. These elements add point masses to these locations without adding any stiffness. The 90° orientation allows for more node lines to be affected. At the higher frequencies, the node lines are more sparsely scattered across the patch region, which would lessen this effect.

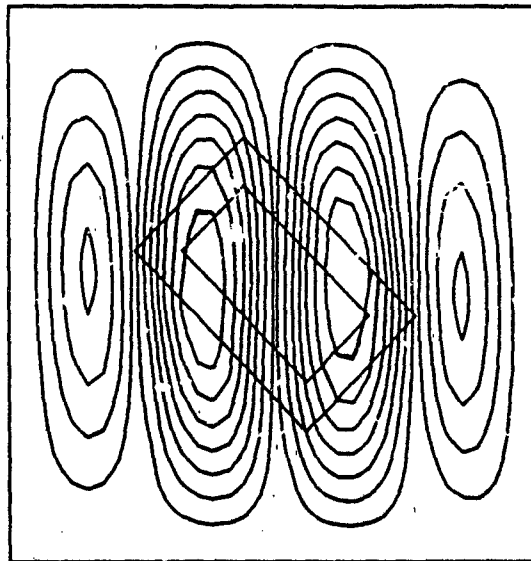
+45° REPAIRED PANEL MODEL. These models behaved very much as expected, and they are very similar to the next set, as would be expected from symmetric repairs to a quasi-isotropic laminate. The frequency results are shown in Table 13.

Table 13. +45° Repair Model Results

	f_1	f_2	f_3	f_4	f_5
Rivet Model	488	510	737	799	854
Goodwin Exp. (GE)	506	525	721	789	820
% Difference	-3.56%	-2.86%	+2.22%	+1.27%	+4.15%
Perfect Bond Model	559	583	783	886	917
% Diff. vs GE	+10.5%	+11.0%	+8.60%	+13.3%	+11.8%

(* all frequencies are in hertz)

The mode shapes themselves are also well-behaved, except for a mode switch between the fourth and fifth modes of both of these models with respect to Goodwin's experimental mode shapes. Since the mode shapes shown in Figures 88 through 97 match those of the undamaged panel, they are believed to be arranged in the proper order.



**Figure 88. +45° Repair Individual Rivet Model
Mode 1, $f = 488$ hz**

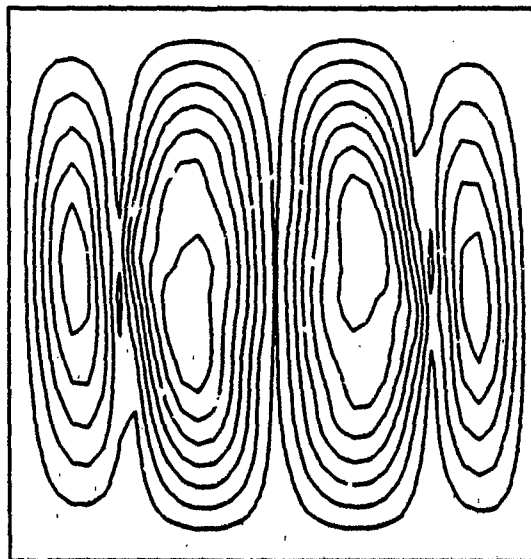


**Figure 89. +45° Repair Perfect Bond Model
Mode 1, $f = 559$ hz**

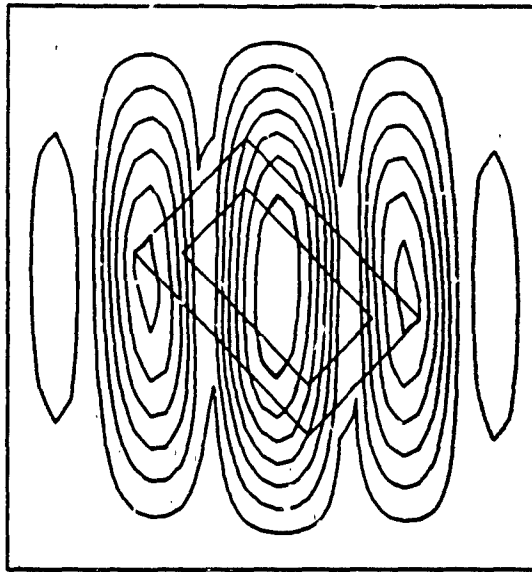


**Figure 90. +45° Repair Individual Rivet Model
Mode 2, $f = 510$ hz**

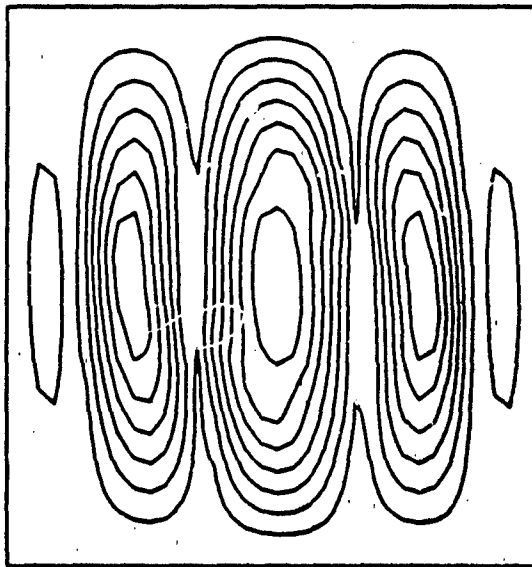


**Figure 91. +45° Repair Perfect Bond Model
Mode 2, $f = 583$ hz**

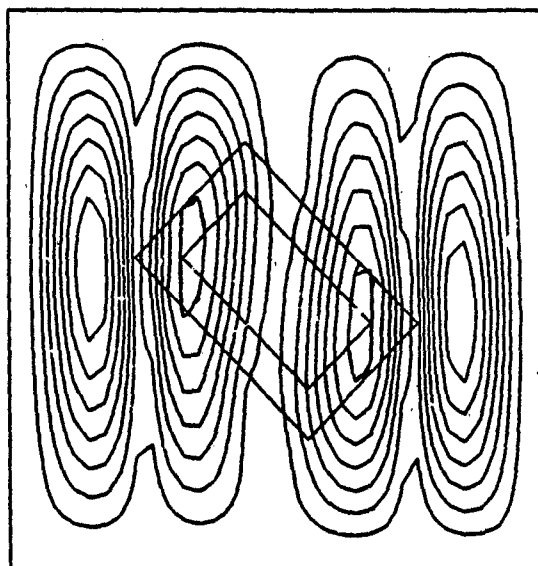


**Figure 92. +45° Repair Individual Rivet Model
Mode 3, $f = 737$ hz**

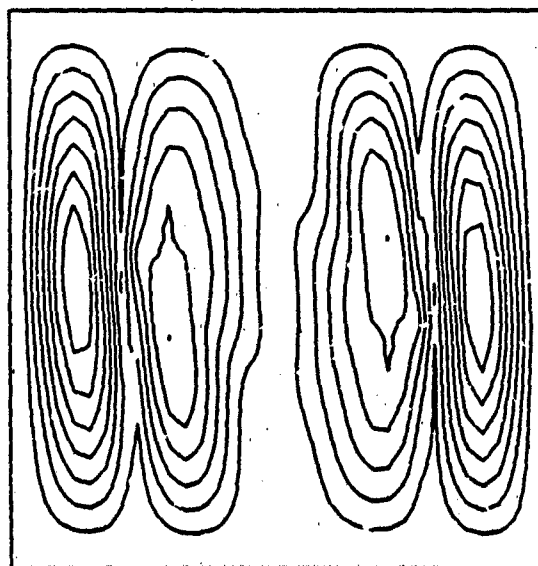


**Figure 93. +45° Repair Perfect Bond Model
Mode 3, $f = 783$ hz**

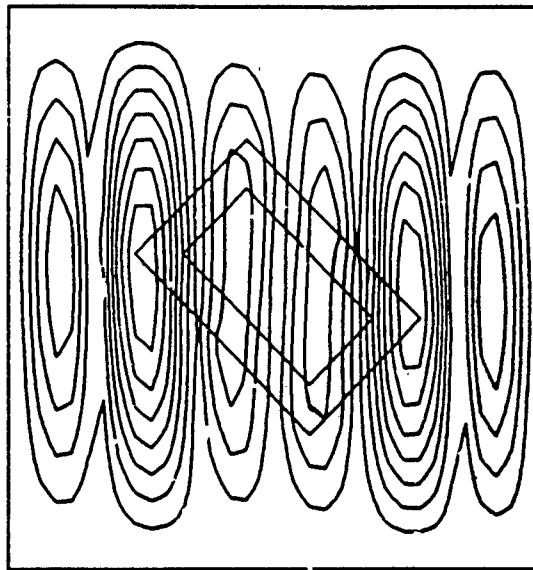


Figure 94. +45° Repair Individual Rivet Model
Mode 4, $f = 799$ hz

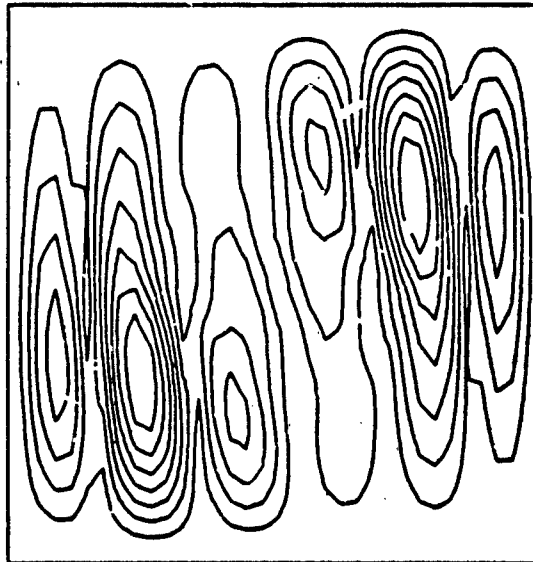


Figure 95. +45° Repair Perfect Bond Model
Mode 4, $f = 886$ hz

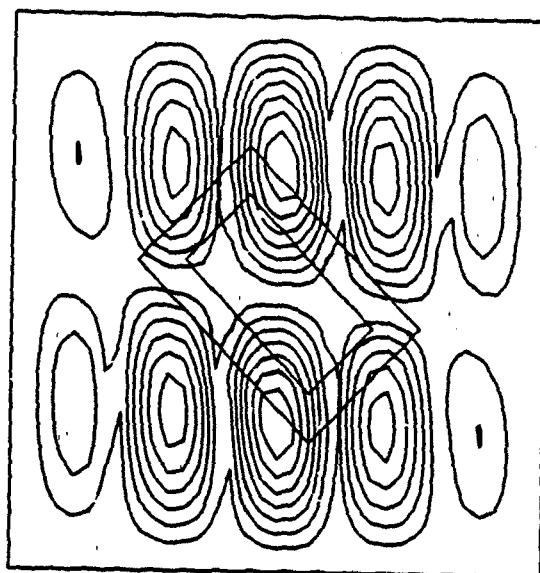


Figure 96. +45° Repair Individual Rivet Model
Mode 5, $f = 854$ hz

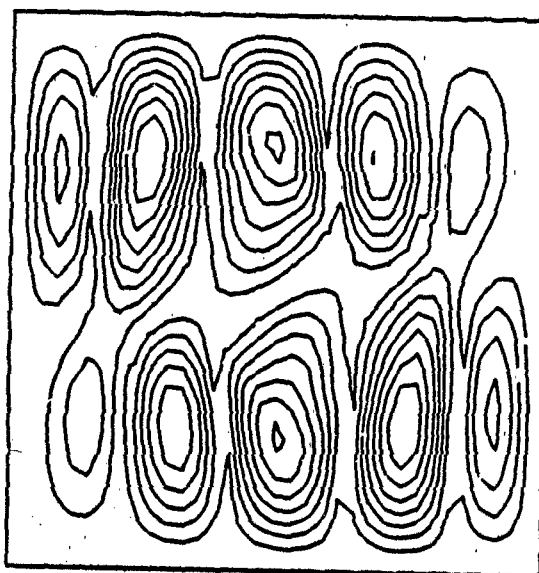


Figure 97. +45° Repair Perfect Bond Model
Mode 5, $f = 917$ hz

The graph in Figure 98 show that for the first two natural frequencies the individual rivet model are lower than those reported by Goodwin for his experimental work.

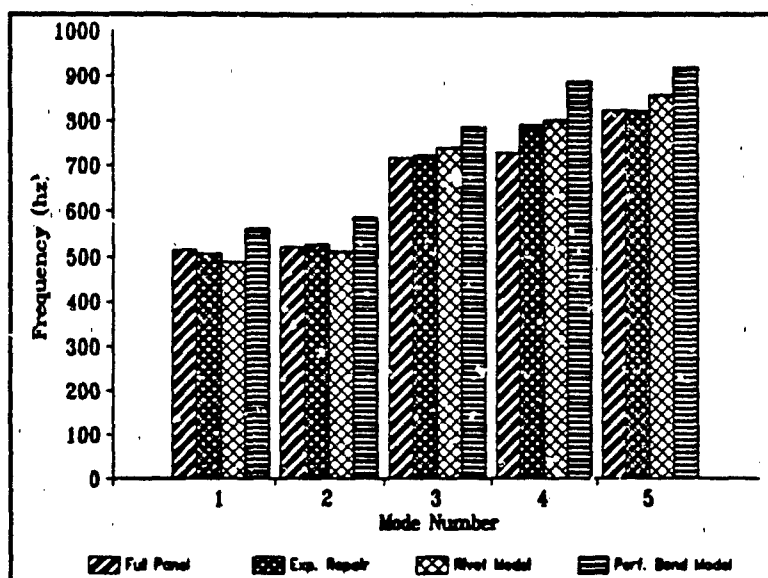


Figure 98. +45° Repair Effects

This is the same behavior exhibited by the 90° repaired panel model, though to a lesser extent. Since this patch is oriented halfway between the 0° and 90° patch, the behavior of this model should reflect aspects of both.

-45° REPAIRED PANEL MODEL. This results from this model are very similar to the preceding one, as previously stated. The frequency results are shown in Table 14.

Table 14. -45° Repair Model Results

	f_1	f_2	f_3	f_4	f_5
Rivet Model	476	513	702	775	842
Goodwin Exper. (GE)	505	516	717	750	806
% Difference	-5.74%	-0.581%	-2.09%	+3.33%	+4.46%
Perfect Bond Model	608	642	831	943	948
% Diff. vs GE	+20%	+24%	+16%	+26%	+18%

(* all frequencies are in hertz)

The mode shapes for the individual rivet model agree with those from Goodwin's experimental work, but the fourth and fifth mode shapes of the perfect bond model are indistinct and cannot be accurately identified. The mode shapes are shown in Figures 99 through 108.

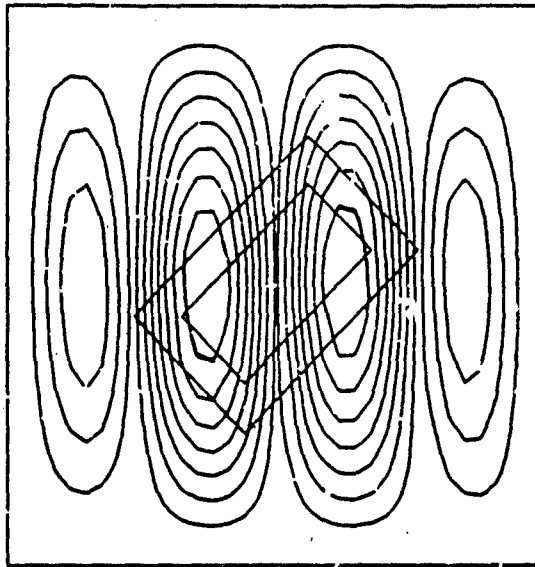


Figure 99. -45° Repair Individual Rivet Model
Mode 1, $f = 476$ hz

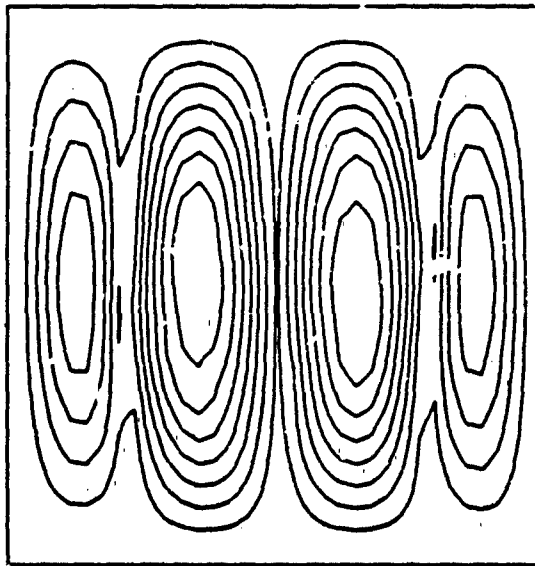
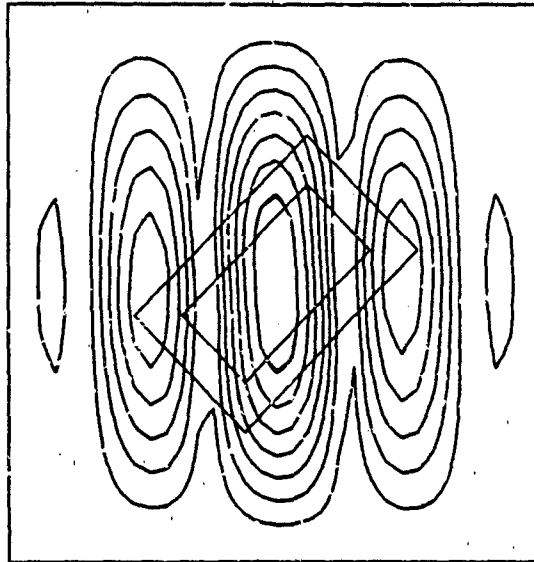
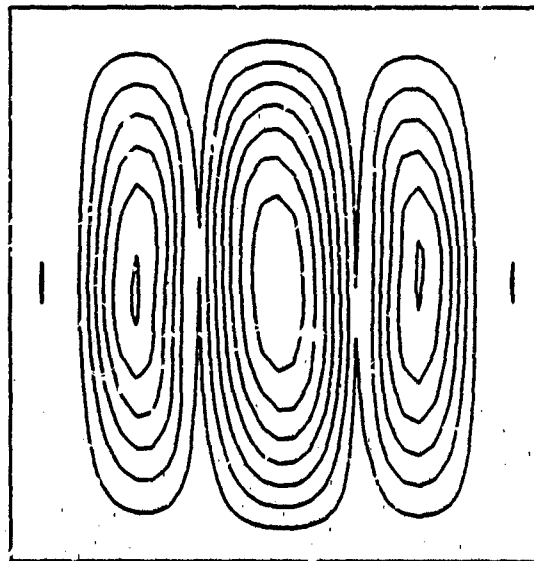


Figure 100. -45° Repair Perfect Bond Model
Mode 1, $f = 608$ hz



**Figure 101. -45° Repair Individual Rivet Model
Mode 2, $f = 513$ hz**



**Figure 102. -45° Repair Perfect Bond Model
Mode 2, $f = 642$ hz**

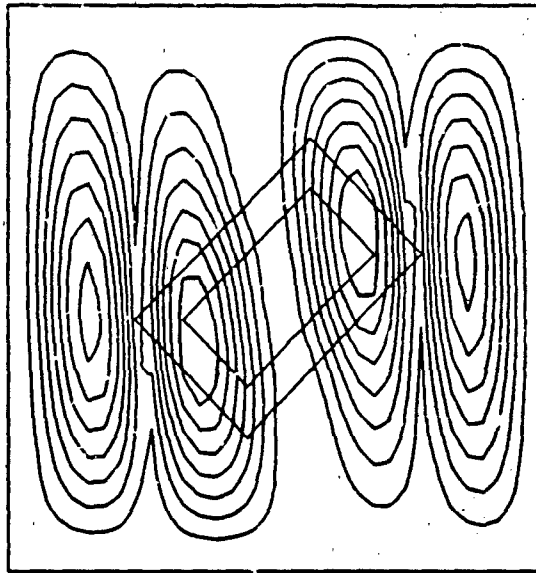


Figure 103. -45° Repair Individual Rivet Model
Mode 3, $f = 702$ hz

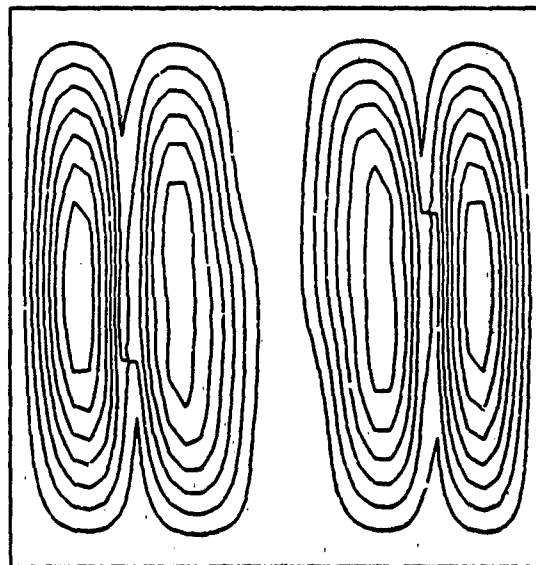
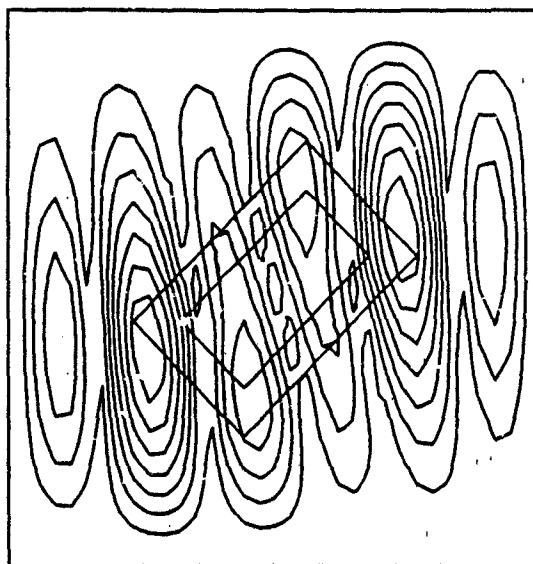
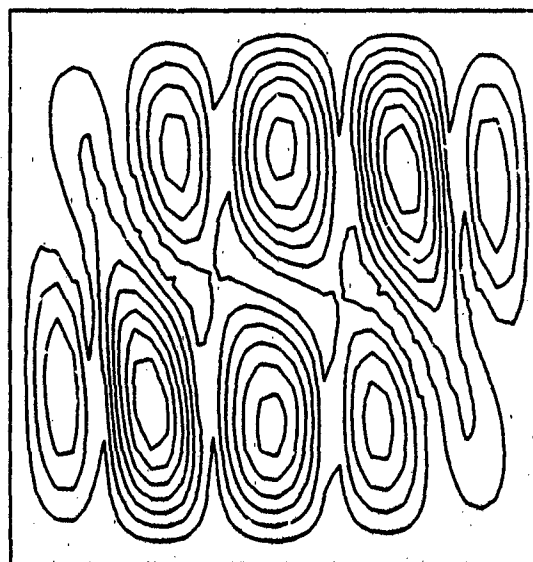


Figure 104. -45° Repair Perfect Bond Model
Mode 3, $f = 831$ hz



**Figure 105. -45° Repair Individual Rivet Model
Mode 4, $f = 775$ hz**



**Figure 106. -45° Repair Perfect Bond Model
Mode 4, $f = 943$ hz**

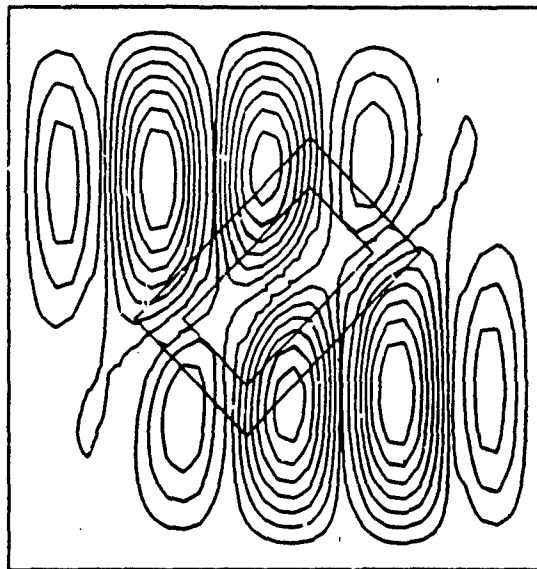


**Figure 107. -45° Repair Individual Rivet Model
Mode 5, $f = 842$ hz**

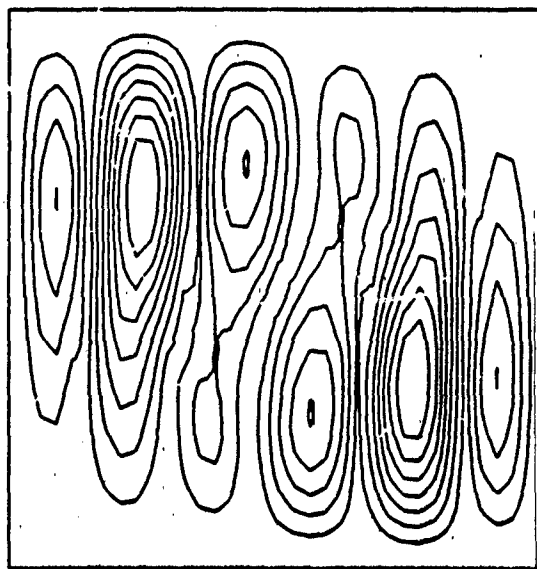


**Figure 108. -45° Repair Perfect Bond Model
Mode 5, $f = 948$ hz**

The graphic comparison shown in Figure 109 is very similar to Figure 98, as expected.

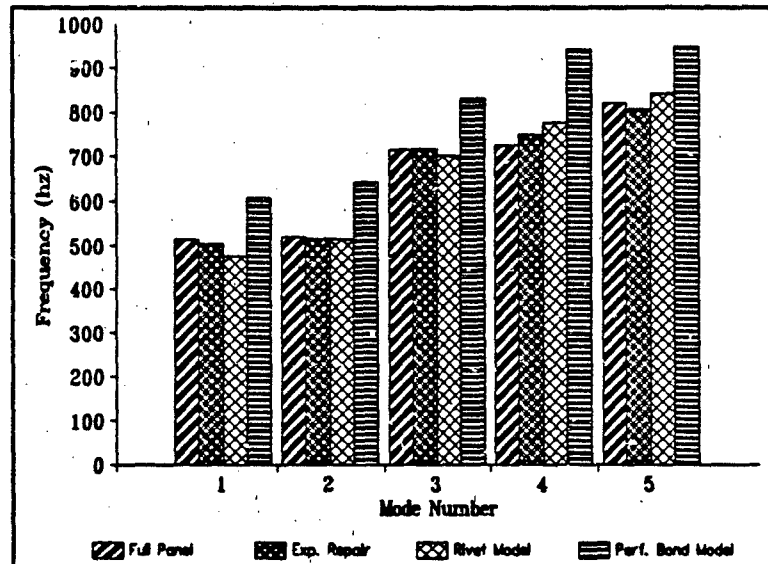


Figure 109. -45° Repair Effects

The individual rivet model follows the trend of the experimental work by Goodwin, whereas the perfect bond model is consistently high.

V CONCLUSIONS AND RECOMMENDATIONS

This thesis has shown that a curved rectangular composite panel modeled with flat MSC/NASTRAN QUAD4 elements can be successfully modified to show the effect of a cutout region and subsequent repair on the dynamic behavior of the panel. More specifically, using ELAS2 and CONM2 elements to model the individual rivets in conjunction with GAP elements to model the separation of the midsurfaces of the panel and the repair allowed a much more accurate prediction of the first five natural frequencies of the repaired panel than did a model assuming a perfect bond between the patch and the panel. The individual rivet model also was better able than the perfect bond model to predict accurately the first five mode shapes of the repaired panel, with the exception of the occasional switch between the fourth and fifth mode shapes. It was able to show the effect of the rivets on the mode shapes, whereas the perfect bond model was not.

The occurrence of mode switching in these models is not believed to be important, though. The mode switching only occurs between the higher mode shapes, which are of less relevance than the first. Also, since mode switching is experienced in experimental models as well and analytical ones, it is likely to be encountered outside the laboratory and should not be

ignored.

For further research in this area, the static failure modes of a repaired panel should be investigated, both experimentally and analytically. Along a similar vein, the effect of the riveted repair on the buckling behavior of the repaired panel should be investigated.

It is unlikely that the future of ABDR will rest with riveted repairs. The advances being made with low temperature, fast-curing adhesives make it seem probable that they will see more use in field repairs. Therefore, the dynamic behavior of such a repair should be investigated, as well as its failure modes and the its effect on the buckling behavior of the panel.

BIBLIOGRAPHY

1. Application Manual, MSC/NASTRAN, Volumes I and II. Los Angeles: The MacNeal Schwendler Corporation, 1982.
2. Ashton, J. E., and others. Primer on Composite Materials: Analysis. Stamford, Conn: Technomic Publishing Co., 1969.
3. Cook, Robert D., and others. Concepts and Applications of Finite Element Analysis (Third Edition). New York: John Wiley and Sons, 1989.
4. Cyr, Capt. Garry J. Effect of Cutout Orientation on Natural Frequencies and Mode Shapes of Curved Rectangular Composite Panels. Master's Thesis, AFIT/GAE/AA/86D-3. School of Engineering, Air Force Institute of Technology (AU), Wright-Patterson Air Force Base, Ohio, December 1986.
5. Cyr, Capt. Garry J., R. L. Hinrichsen, and Capt. R. A. Walley. "Effect of cutout on the Dynamic Response of Curved Rectangular Composite Panels," AIAA Journal, Vol. 26, No. 5: 582-588 (May 1988).
6. Gans, Capt. Howard D. and others. "Effects of Battle Damage Repair on the Natural Frequencies and Mode Shapes of Curved Rectangular Composite Panels," AIAA 32nd Structures, Structural Dynamics, and Materials Conference. 3026-3038. Washington, D. C.: AIAA Press, 1991
7. Goodwin, Maj. William P. Effects of Battle Damage Repair on the Natural Frequencies and Mode Shapes of Curved Rectangular Composite Panels. Master's Thesis, AFIT/GAE/AA/88D-18. School of Engineering, Air Force Institute of Technology (AU), Wright-Patterson Air Force Base, Ohio, December 1988.
8. Mariquez, Ted, and others. "Refinement of Finite Element Model of Thin Interfaces using Experimental Modal Analysis for Comparison," Proceedings of the 6th International Modal Analysis Conference: February 1-4, 1988. 428-431.
9. Hinkle, T. and Van Es, J. Battle Damage Repair of Composite Structures. AFWAL-TR-87-3104. Air Force Wright Aeronautical

Laboratories, Air Force Systems Command, Wright Patterson Air Force Base, Ohio, March 1988.

10. Hurty, Walter C. and Moshe F. Rubinstein. Dynamics of Structures. Englewood Cliffs, NJ: Prentice-Hall, Inc. 1964.
11. Jones, Robert M. Mechanics of Composite Materials. New York: Hemisphere Publishing Corporation, 1985.
12. Levraea, Capt. Vincent J., Jr. Eccentricity Effects of Square Cutouts on the Natural Frequencies and Mode Shapes of Curved Rectangular Composite Panels. Master's Thesis, AFIT/GAE/ENY/89D-20, School of Engineering, Air Force Institute of Technology (AU), Wright-Patterson Air Force Base, Ohio, December 1989.
13. Logan, Daryl L. A First Course in the Finite Element Method. Boston: PWS-Kent Publishing Co., 1986.
12. MacNeal, Richard H. "A Simple Quadrilateral Shell Element," Computers and Structures, Vol. 8: 175-183 (Pergamon Press, 1978).
13. Meirovitch, Leonard. Elements of Vibration Analysis (Second Edition). New York: McGraw-Hill Book Company, 1986.
14. Rajamani, A., and R. Prabhakaran. "Dynamic Response of Composite Plates with Cut-Outs, Part II: Clamped-Clamped Plates," Journal of Sound and Vibration, 54-4: 565-576 (22 October 1977).
15. Rao, S. S. The Finite Element Method in Engineering. New York: Pergamon Press, 1982.
16. Sanders, A. L., and others. Rapid Repair of Battle Damaged Aircraft Structures: Final Report, September 1980 - January 1984. AFWAL-TR-84-3034. Air Force Wright Aeronautical Laboratories, Air Force Systems Command, Wright-Patterson Air Force Base, Ohio, May 1985.
17. Strang, Gilbert and George C. Fix. An Analysis of the Finite Element Method. Englewood Cliffs, NJ: Prentice-Hall, Inc., 1973.
18. Theoretical Manual, MSC/NASTRAN. Los Angeles: The MacNeal Schwendler Corporation, 1985.

19. Tse, Francis S., and others. Mechanical Vibrations, Theory and Applications (Second Edition). Boston: Allyn and Bacon, 1979.
20. Vinson, J. R. and R. L. Sierakowski. The Behavior of Structures Composed of Composite Materials. Dordrecht, Netherlands: Martinus Nijhoff Publishers, 1986.
21. Walley, Capt. Richard A. Natural Frequencies and Mode Shapes of Curved Composite Panels with Interior Cutouts. Master's Thesis, AFIT/GAE/AA/85D-16. School of Engineering, Air Force Institute of Technology (AU), Wright-Patterson Air Force Base, Ohio, December 1986.

Vita

Scott A. Hamilton was born on 30 March 1968 in Knoxville, Tennessee. In May of 1986 he graduated from Germantown High School in Germantown, Tennessee and entered the U. S. Air Force Academy that June. In May of 1990 he graduated with a Bachelor of Science in Engineering Mechanics. Upon graduation, he received a regular commission in the USAF and a sudden, overwhelming realization that he needed to strive for yet a higher level of education, so he entered the School of Engineering, Air Force Institute of Technology, in July 1990.

REPORT DOCUMENTATION PAGE			Form Approved OMB No. 0704-0188	
<small>Public reporting burden for this collection of information is estimated to average 1 hour per response, including the time for reviewing instructions, searching existing data sources, gathering and maintaining the data needed, and completing and reviewing the collection of information. Send comments regarding this burden estimate or any other aspect of this collection of information, including suggestions for reducing this burden, to Washington Headquarters Services, Directorate for Information Operations and Reports, 1215 Jefferson Davis Highway, Suite 1204, Arlington, VA 22202-4302, and to the Office of Management and Budget, Paperwork Reduction Project (0704-0188), Washington, DC 20503.</small>				
1. AGENCY USE ONLY (Leave blank)		2. REPORT DATE December 1991		3. REPORT TYPE AND DATES COVERED Master's Thesis
4. TITLE AND SUBTITLE FINITE ELEMENT ANALYSIS OF A RIVETED REPAIR ON A CURVED COMPOSITE PANEL				5. FUNDING NUMBERS
6. AUTHOR(S) Scott Hamilton, 2Lt, USAF				
7. PERFORMING ORGANIZATION NAME(S) AND ADDRESS(ES) Air Force Institute of Technology, WPAFB OH 45433-6583			8. PERFORMING ORGANIZATION REPORT NUMBER AFIT/GAE/ENY/91D-3	
9. SPONSORING MONITORING AGENCY NAME(S) AND ADDRESS(ES) Dr. V. B. Venkayya WL/FIBR Wright-Patterson AFB, OH 45433			10. SPONSORING MONITORING AGENCY REPORT NUMBER	
11. SUPPLEMENTARY NOTES				
12a. DISTRIBUTION / AVAILABILITY STATEMENT Approved for public release; distribution unlimited			12b. DISTRIBUTION CODE	
13. ABSTRACT (Maximum 200 words) A finite element model of a curved composite panel with a center cutout section was developed and verified using previously obtained modal test results. The FEM was modified using different methods to exhibit the effects of riveting an aluminum patch to the panel as a repair on its dynamic behavior. The different methods were contrasted against each other and previously obtained modal results. The first method assumed a perfect bond between the patch and the panel, and used elements with an average of the panel and patch properties to model the region where the patch overlaps the panel. The second method modeled the patch and panel as separate curved surfaces, and modeled the rivets individually. For the perfect bond model, the modes shapes agreed with experimental data at lower frequencies but were distorted at higher ones, and predicted frequencies that were regularly 5-25% high. Modeling the rivets individually produced matching mode shapes and frequencies that were regularly within 5% of experimental values.				
14. SUBJECT TERMS Finite Element Analysis; Composite Structures; Repairs; Locking Fastener Devices; Vibrations; Dynamics			15. NUMBER OF PAGES 107	
			16. PRICE CODE	
17. SECURITY CLASSIFICATION OF REPORT Unclassified	18. SECURITY CLASSIFICATION OF THIS PAGE Unclassified	19. SECURITY CLASSIFICATION OF ABSTRACT Unclassified	20. LIMITATION OF ABSTRACT UL	

**END
FILMED**

DATE:

1-92

DTIC